DOI: 10.1002/ ((please add manuscript number))
Article type: Progress Report

Title Understanding CeO_2-based Nanostructures through Advanced Electron Microscopy in 2D and 3D

Yang Zhang, Sara Bals, and Gustaaf Van Tendeloo*

Dr. Yang Zhang, Prof. Sara Bals, Prof. Gustaaf Van Tendeloo
EMAT, University of Antwerp, Groenenborgerlaan 171, B-2020 Antwerp, Belgium
E-mail: sara.bals@uantwerpen.be

Keywords: CeO_2, catalysis, electron microscopy, electron tomography, mechanism

ABSTRACT: Engineering morphology and size of CeO_2-based nanostructures on a (sub) nanometer scale will greatly influence their performances; this because of their high oxygen storage capacity (OSC) and unique redox properties, which allow faster switching the oxidation state between Ce^{4+} and Ce^{3+}. Although tremendous researches have been carried out on the shape-controlled synthesis of CeO_2, the characterization of these nanostructures at atomic scale remains a major challenge and the origin of debate. The rapid developments of *aberration-corrected* transmission electron microscopy (*AC*-TEM) have pushed the resolution below 1 Å, both in TEM and in STEM mode. At present not only morphology and structure, but also composition and electronic structure can be analysed at an atomic scale, even in three dimensions (3D). This review summarizes recent significant achievements using TEM/STEM and associated spectroscopic techniques to study CeO_2-based nanostructures and related catalytic phenomena. Recent results have shed light on the understanding of the different mechanisms. The potential and limitations including future needs of various techniques are discussed with recommendations to facilitate further developments of new and highly efficient CeO_2-based nanostructures.

1. Introduction

Because of its high oxygen storage capacity (OSC) and unique redox properties, CeO_2-based nanostructures have widespread applications such as, oxygen sensors, solid oxide fuel cells (SOFCs), water-gas-shift (WGS) reaction, three-way catalysts (TWCs), UV shielding, water treatment and biomedicine.[1] With the rapid developments of nanoscience and nanotechnology over the past decades, it is now possible to prepare CeO_2 nanomaterials with a variety of morphologies like spheres, rods, wires, tubes and cubes. This know-how is a prerequisite for targeting the correlation between specific morphology and catalytic efficiencies.[1f, 2] Indeed, size, morphology, chemical composition and valence state of CeO_2 play a critical role in determining its catalytic performance.[1f, 3] Therefore, it is essential to characterize these parameters at an atomic scale, particularly in three dimensions (3D).

Because of its superior imaging resolution, transmission electron microscopy (TEM) and/or scanning TEM (STEM) have long been the primary characterization technique used for studying nanostructures.[4] Especially, the rapid development of both aberration correctors and monochromators, have significantly improved the spatial and energy resolution. Imaging atomic structures with sub angstrom resolution and identifying chemical compositions with single-atom sensitivity are now more or less routine for *aberration-corrected* TEM/STEM (*AC*-TEM/STEM). Currently, a sub angstrom resolution is achieved both in TEM and in STEM; this allows imaging single atoms as well as energy dispersion X-ray spectroscopy (EDX) or electron energy loss spectroscopy (EELS) on a single atomic column.[4c, 5] However, one should never forget that conventional TEM/STEM techniques only provide two-dimensional (2D) projections of three-dimensional (3D) objects.[6] It is therefore important to expand these investigations into 3D, especially for nanocatalysts. CeO_2-based nanostructures have a higher catalytic activity for the (100) and (110) surfaces compared to the (111) surface, and therefore the exact 3D morphology is of uttermost importance.[1f, 2a] Electron tomography is a technique

to create a 3D reconstruction out of a tilt series of 2D projection images. Electron tomography not only provides atomic scale information on the 3D morphology; in combination with spectral techniques such as EDX or EELS it also provides information on composition and valence state.[6a, 6b, 7] Therefore, electron tomography has become a versatile tool to study the correlation between composition, structure and properties of nanostructures.

Because of its high importance, several reviews on the controlled synthesis, properties and applications of CeO_2-based nanostructures have been published.[1a, 1c, 1d, 1f] For example, Sun et al. reviewed the progress in the synthesis of various morphologies of CeO_2 and selected applications.[2a] Trovarelli et al. summarized the correlation between surface properties, crystal size, and morphologies of the three most common ceria shapes (nanopolyhedra, nanorods, and nanocubes) in the absence and presence of an active metal phase.[1f] Wu et al. focused on the synthesis of CeO_2-based nanostructures with different morphologies and their related energy and environment applications.[1a] Montini et al. provided a general and ample view on the properties of CeO_2-based nanostructures and applications.[1c] However, most of these reviews solely focused on the controlled synthesis of various morphologies of CeO_2-based nanostructures for widespread applications and much less on the understanding of the composition-structure-property relationship. The recent and exciting developments in TEM/STEM, however, have opened new possibilities for the characterization of nanostructures, in particular for CeO_2-based nanostructures.[4b, 4c, 5a, 8]

In the present review, we focus on the progress made over the past decade towards the understanding of CeO_2-based nanostructures and the catalysis mechanisms through advanced TEM techniques. Apart from addressing the basic physical and chemical properties of CeO_2-based nanostructures, emphasis is given to the contribution of TEM/STEM to study these nanostructures and we will highlight the recent developments of in-situ TEM. The next part discusses the use of high-angle annular dark-field HAADF-STEM and EELS-STEM for 3D

morphology and valence state characterization. We conclude this review with critical comments, as well as some perspectives on future developments for a full characterization of CeO_2-based nanostructures.

2. CeO_2-based Nanostructures: General Overview

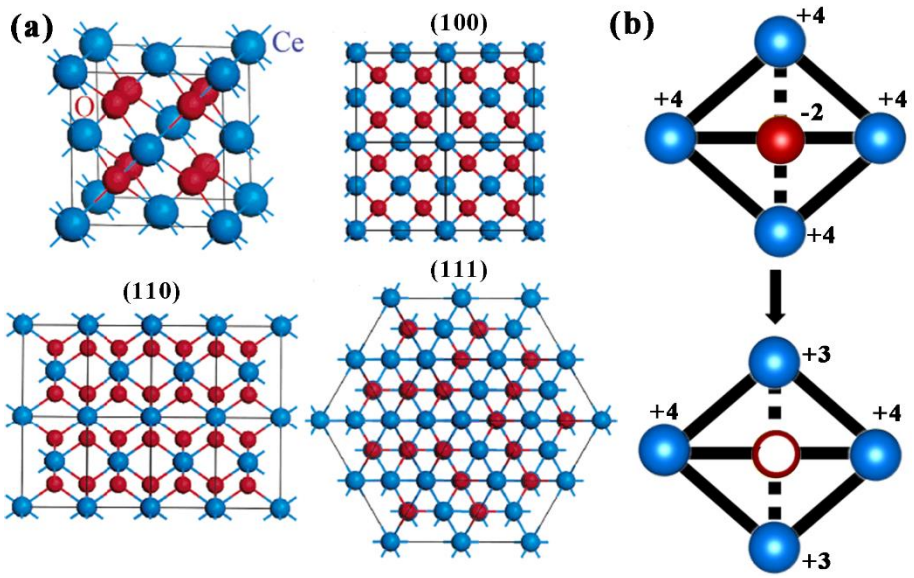

Figure 1. (a) Unit cell and the (100), (110), and (111) projections of the CeO_2 structure. (b) Schematic of the standard picture of charge redistribution following the formation of an oxygen vacancy in CeO_2. Ce atoms (blue circles), O atom (red circle), neutral O vacancy (empty circle). Reproduced with permission.[9] Copyright 2003, American Chemical Society.

Crystalline CeO_2 has a cubic fluorite structure with lattice constant a = 5.41134 Å and space group $Fm\bar{3}m$.[1a, 2a, 9] The fluorite structure consists of a face-centred cubic (fcc) unit cell of cerium cations, which are coordinated by eight nearest-neighbour oxygen anions, while each oxygen anion is coordinated by four nearest-neighbour cerium cations, occupying the octahedral interstitial sites, as depicted in Figure 1a. A cerium cation in CeO_2 has the ability to easily switch oxidation state between Ce^{4+} and Ce^{3+} depending on whether it is present in an oxidizing or reducing environment (Figure 1b), with the concomitant formation of oxygen vacancies; this can be expressed by the Kroger-Vink notation,[1c, 10]

$$2Ce_{Ce} + O_O \rightarrow V_O^{\cdot\cdot} + 2\mathrm{Ce}'_{Ce} + \frac{1}{2}O_2 \quad (1)$$

Oxygen vacancies are mobile active sites which can act as centres for oxidation and reduction reactions. This is connected with the OSC of CeO_2, which is the intrinsic property for potential applications in energy conversion, catalysis, biomedical applications, etc.[1b, 1c, 11]

Most studies focused on the three thermodynamically most stable surfaces (111), (110) and (100) of CeO_2.[12] It should be pointed out that for these surfaces the coordination number is lower than in the bulk (8 for Ce^{4+} and 4 for O^{2-}), which points towards more active surfaces.[1a, 1f] Experimental and theoretical studies have proven that the vacancy formation energy is different for these surfaces, following the order of (110)＜(100)＜(111).[1f, 12b, 13] Surface reducibility, an important intrinsic characteristic of CeO_2, is closely related to its catalytic properties that are reflected by the vacancy formation energy. Therefore, the (100) and (110) surfaces of CeO_2 are more reducible and active than the (111) surface.

3. Electron Microscopy Characterization of CeO_2-based Nanostructures

3.1 Basic information

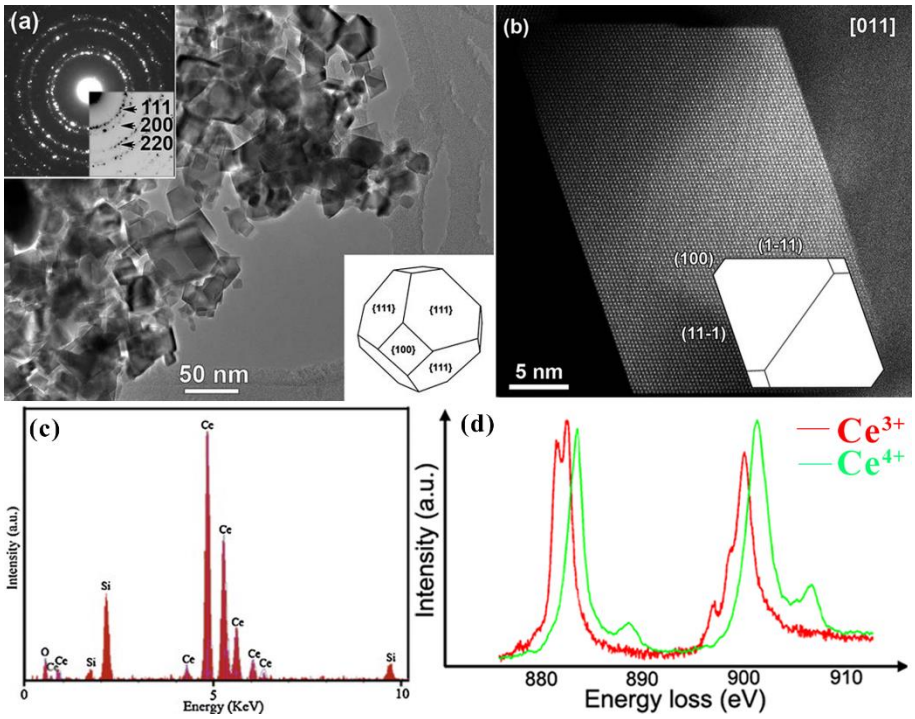

Figure 2 Various basic TEM/STEM techniques applied to CeO_2 research. TEM, electron diffraction (ED) (a) and HAADF-STEM image (b) of CeO_2 nanoparticles. (c) EDX spectrum of CeO_2 showing the chemical composition. (d) EELS spectroscopy for Ce^{4+} and Ce^{3+}. Reproduced with permission.[14] Copyright 2011, Royal Society of Chemistry; copyright 2015, Elsevier; and copyright 2014, American Chemical Society.

Apart from classical imaging by TEM and electron diffraction (Figure 2a), novel techniques are now available for the characterization of CeO_2-based nanostructures. STEM in combination with EDX/EELS for composition and valence state analysis is an extremely powerful technique that has been fully explored recent years (Figure 2b, c, d).[2d, 14-15] Through this combined information the morphology, crystal structure, particle size distribution, composition and electronic information on CeO_2-based nanostructures can be obtained.

3.2 Surface structure

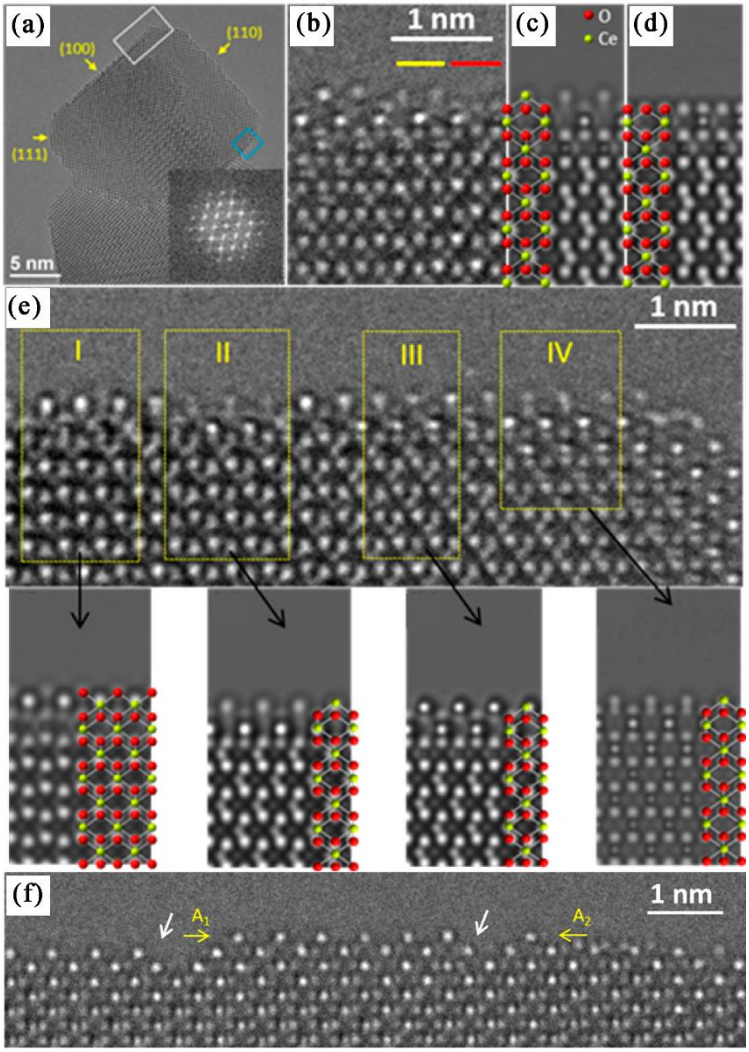

Figure 3 (a) HRTEM image on a typical CeO_2 nanocube along the [110] zone axis with the FFT of the region of interest (the area highlighted by the white box) shown as inset. (b) A magnified HRTEM image of the (100) surface in the blue box in (a). (c, d) Simulated HRTEM images to be compared with (b) using Ce and O terminations respectively. (e) Magnified HRTEM image of the (100) surface in the white box of (a), together with the simulated images for different surface configurations. (f) HRTEM image of the (110) surface of a CeO_2 nanocube along the [110] zone axis. The white arrows indicate (111) nanofacets. Reproduced with permission.[16] Copyright 2013, American Chemical Society.

For catalytic applications, most of the CeO_2-based nanostructures are in the nanometer scale, which results in an increased challenge for surface chemistry in comparison with the bulk.[3e, 4k, 13a, 17] As a consequence the atomic features of the CeO_2 surface are extremely important. Benefiting from the recent developments of *AC*-(S)TEM, remarkable achievements have been obtained in surface exploration, enabling a better understanding of the surface selective catalytic reactions.[5c, 16, 18] Lin et al. successfully observed the O and Ce atom columns on CeO_2 {100}, {110} and {111} surfaces, as presented in Figure 3. The predominantly exposed {100} surfaces have complex mixed terminations with Ce-, O-, and CeO- on the outermost surface (Figure 3b-e). In addition, atom hopping is observed on {100} surfaces. The {110} surfaces show a high density of CeO_{2-x} layers (oxygen vacancies) and easily form {111} nanofacets to lower the surface energy (Figure 3f). The {111} surfaces are always truncated with an O termination. Haigh et al. also studied several low index surfaces of CeO_2 using a combination of *AC*-TEM and computational exit wave function reconstruction. They find that {111} surfaces are stabilized by O termination, while {100} surfaces are unstable.[19]

Recently, a metastable surface was described by Huang et al. on the CeO_2 {100} surfaces (Figure 4).[20] The atomic relaxation is less than 0.2 Å for the normal Ce- and O-terminated {100} surfaces. However, a surprisingly huge surface relaxation was revealed for the outermost Ce layer and the Ce sublayer. In comparison with the normal Ce-terminated surface, this new structure has the same surface stoichiometry but the original O sublayer moved across the original Ce outermost layer, resulting in a reversed structure with O termination. These results indicate that the surface of CeO_2 nanostructures can be far more complex than previous simple assumptions. These different surface structures on {100}, {110} and {111} surfaces certainly influence the morphology dependent catalytic properties.

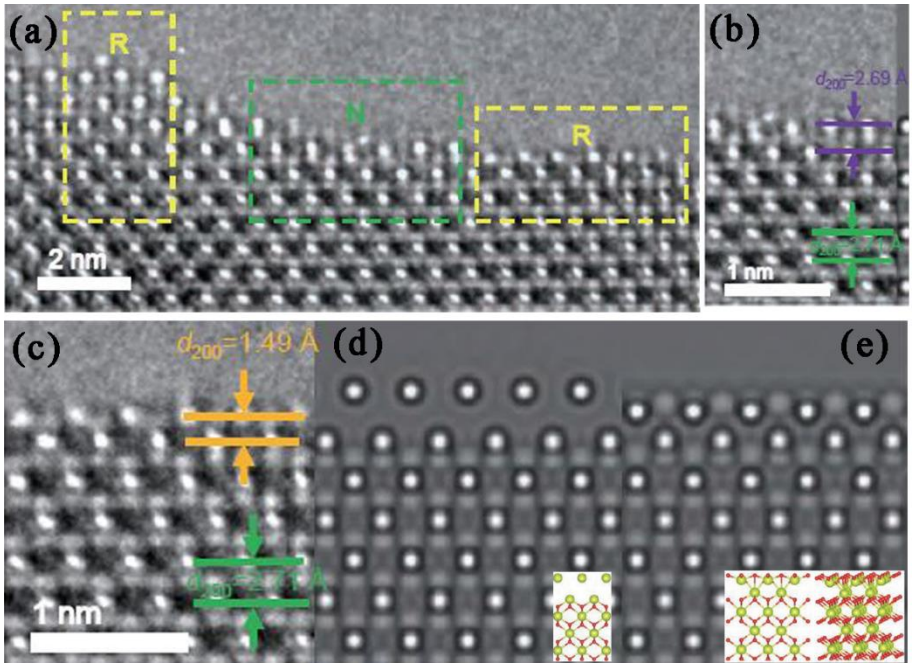

Figure 4 (a) Experimental HRTEM image of a CeO_2 (100) surface, viewed along the [011] zone axis. (b) Enlarged image of the (100) surface of CeO_2, showing a slight inward relaxation of the surface layers. (c) Enlarged image of the reversed (100) surface of CeO_2, with a huge inward relaxation of the outermost Ce layer. (d, e) Simulated images relaxed using first-principles calculations together with the corresponding models. Reproduced with permission.[20] Copyright 2017, Springer Nature.

3.3 Dynamics and reconstruction of surfaces

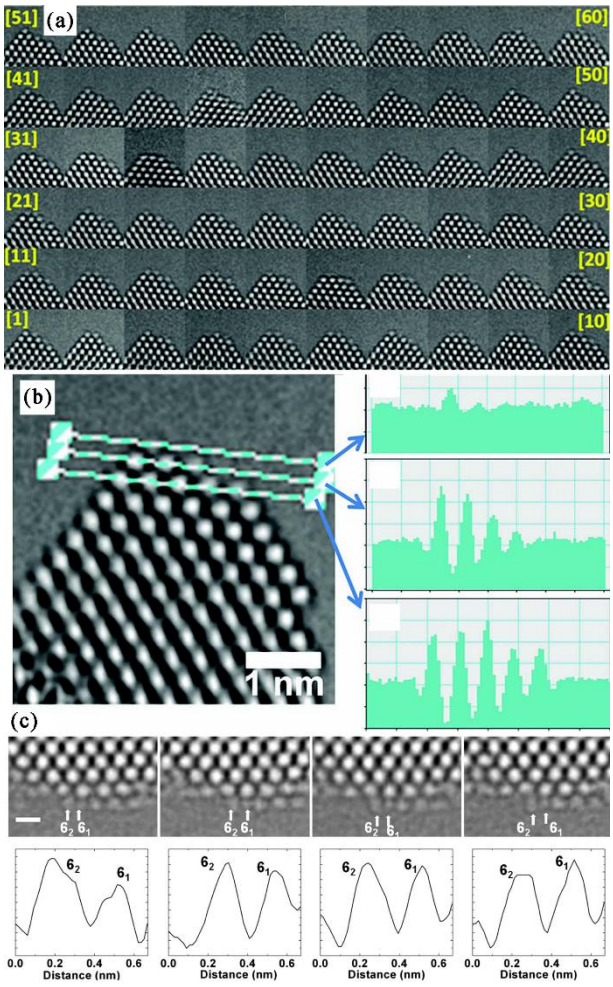

Figure 5 (a) a series of TEM images of a CeO_2 nanoparticle, recorded with 2 s intervals. Frames are numbered from 1 to 60. (b) Magnified image from frame 26 with three line profiles of 3.3 nm length along {100} across the first, second, and third monolayer; the intensity variations are plotted next to it. (c) Magnified images of the {100} surface and profile plots of two positions (6_1 and 6_2) of the outer layer, corresponding to 20 s, 30 s, 32 s, and 34 s. It illustrates the surface reconstruction of two projected atomic positions occupying one bulk lattice Ce site. Scale bar = 0.5 nm. Reproduced with permission.[21] Copyright 2011, Wiley; copyright 2012, American Chemical Society.

As the catalytic efficiency of CeO_2-based nanostructures is closely related to its surface structure, it is important to design nanocatalysts with a maximum of active surfaces. But as

nanofaceting, surface reconstruction and surface vacancies may appear on the different facets, they could affect the stability and the catalytic performance. Therefore, it is crucial to take all these factors into account when constructing the structure-catalysis relationship.[1f, 17c, 22] The binding energy of the Ce and O atoms to the surface will reflect the mobility and catalytic activity. Computer simulations suggest that it is easier to extract oxygen from {110} planes than from {111} planes.[23] However, it is still a big challenge to image these atomic arrangements and correlate the dynamic surface changes with the simulations. *AC*-TEM not only improves the point resolution, but also the signal to noise ratio by eliminating blurring and delocalization effects, which makes imaging of single-atom dynamics possible for CeO_2.

Möbus et al. recorded single-atom movements and spontaneous relocations of entire atomic rows on CeO_2 {100} and {111} surfaces (Figure 5).[21a] During the experiments, the {111} surfaces are quite stable at all irradiation doses, while discontinuous and randomly atomic hopping processes are taking place on {100} surfaces. In addition, a Ce atom was irreversibly ablated in the fourth position of the second top layer, while a fluctuation of plus/minus one occupied atom position was observed in both top layers (Figure 5a). The image contrast was fully quantified by the assumption that the lateral particle width was equal to the width along the viewing direction. Correspondingly, single Ce atom contrast features are demonstrated in Figure 5b. Frames 54-56 and 21-25 are typical rearrangements via time-resolved single atom movements, while jumps of entire columns are revealed by frames 3-4 and 36-37. It should be pointed out that no major Ce loss, caused by electron beam ablation, is observed over the complete time series of 120 s. The atomic rearrangements seem to be random and unpredictable, but reversible. Later, Bhatta et al. demonstrated that atomic movements happen across wide {100} surfaces, extending their earlier findings that these movements are confined to one tiny {100} surface.[21b] Cationic surface reconstruction appears in some areas near steps or corners of {100} surfaces, such that two image spots occupy one bulk Ce site (Figure 5c).

3.4 Surfaces reduction

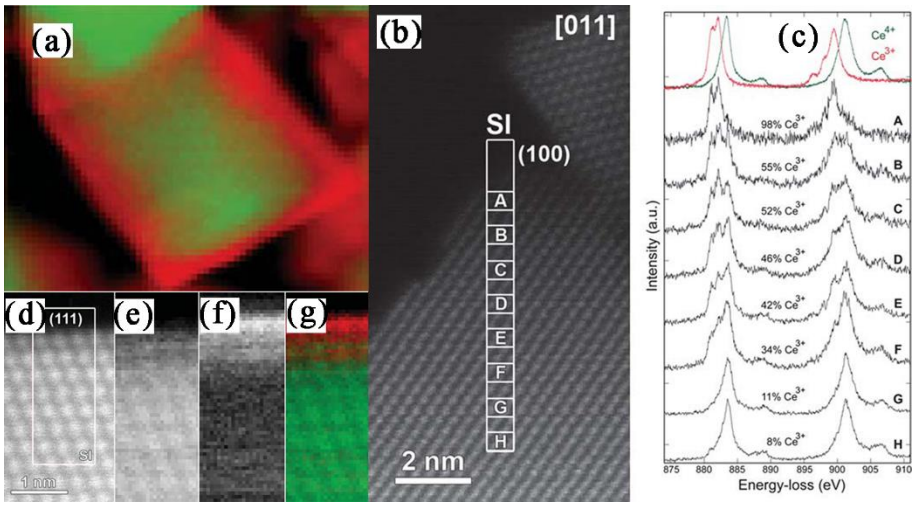

Figure 6 (a) STEM-EELS colour map of CeO_2 nanoparticles with Ce^{3+} (red) and Ce^{4+} (green). (b) HAADF-STEM image showing the (100) surface truncation and the 3*36 pixel SI scan region indicated. (c) Averaged Ce $M_{4,5}$ spectra from regions A-H (3*3 pixels) together with reference spectra for Ce^{3+} and Ce^{4+}. The fitted weight of Ce^{3+} is given for each spectrum. High resolution HAADF-STEM image showing the (d) (111) surface and the 24*59 pixel SI scan region. (e) Ce^{4+} map. (f) Ce^{3+} map. (g) Colour map with Ce^{3+} (red) and Ce^{4+} (green). Reproduced with permission.[14a] Copyright 2011, Royal Society of Chemistry.

An important feature of CeO_2-based nanostructures is the change of the Ce valence from Ce^{4+} to Ce^{3+}, especially on or near the surface; this is due to oxygen vacancies and the atomic rearrangements, which is the key to the catalytic performance.[3c, 24] In a modern TEM, this information can be obtained by EELS which measures the energy loss associated with electrons as they scatter from different atoms within a sample. In general, composition, valence state and bond distance can be retrieved from the position and the fine structure of the core-level energy loss peaks. Therefore, HAADF-STEM together with spatially resolved EELS is a powerful combination to investigate the surface reduction in CeO_2-based nanostructures.[14a, 14c, 25] Recently, Turner et al. characterized the presence and thickness of the reduced Ce^{3+} shell on

the surface of commercial CeO_2 nanoparticles.[14a] The Ce valence is identified by comparing the measured cerium $M_{4,5}$ edge fine structure to known Ce^{3+} and Ce^{4+} references. In Figure 6a, a whole nanoparticle of 40 nm is scanned to visualize the surface reduction and to provide insight into its homogeneity. Valence maps are generated using the EELSMODEL fitting procedure.[26] It is obvious that the surface reduction shell is present over the whole particle surface, with a 2 nm Ce^{3+} shell. Smaller particles of about 5 nm only show the reduced Ce^{3+} state (right side of Figure 6a). An atomic scale characterization of the Ce^{3+} layer on the {100} and {111} surfaces further indicates that all Ce atoms on the top (100) surface are in a reduced Ce^{3+} state, however the Ce^{4+} signal increases linearly from the surface to the inner part of the nanoparticle. The first 5-6 atomic layers on the (100) surface are all in a reduced Ce^{3+} state, intermixing states of Ce^{3+} and Ce^{4+} appear in the next 5-6 atomic layers (Figure 6c). For the (111) surface, only the top layer is Ce^{3+}, while mixed Ce^{3+} and Ce^{4+} states are present in the second and third layer (Figure 6g). The results for the (111) surface with a surface step and island are consistent with the above conclusion, indicating that steps and surface kinks are active sites for catalytic applications. The {100} surface shows 5-6 atomic planes in a reduced Ce^{3+} state, while the reduced shell on {111} surfaces only extends over 2-3 atomic planes, in agreement with the superior catalytic efficiency of {100} surfaces.[1f]

3.5 Atomic structure of CeO_2 grain boundaries

Grain boundaries (GB) are typical crystal defects that affect the material performance due to an abrupt structure and chemical inhomogeneity.[3h, 27] Therefore, atomic scale determination of the grain boundary structure of CeO_2, a key material used in solid oxide fuel cells, is a prerequisite for understanding the GB-property relationship. Using a (210) Σ5 grain boundary as a model, Hojo et al. investigated the Ce and O sublattices by HAADF-STEM and annual bright-field (ABF) STEM, in combination with EELS and theoretical calculations.[28] The contrast of the HAADF-STEM images is sensitive to the atomic number, allowing direct image

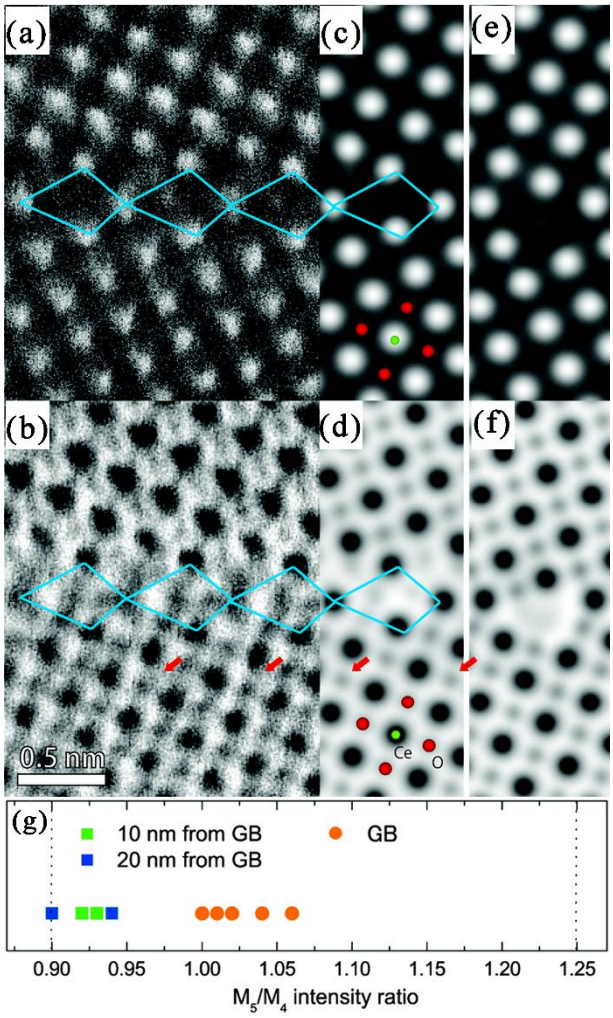

Figure 7 (a) HAADF-STEM and (b) ABF-STEM images of a [001](210)Σ5 grain boundary in a CeO_2 thin film. (c) Simulated HAADF and (d) ABF images of the nonstoichiometric grain boundary model structure. (e) Simulated HAADF and (f) ABF images of the stoichiometric grain boundary model structure. The structural units of each boundary are indicated by polygons. The contrast in (c) and (e) has been aligned a little to fit to the experimental image. (g) Variation of the M_5/M_4 intensity ratio calculated from the positive part of the second derivative of the experimental spectra at several grain boundary regions and grain interior regions. Reproduced with permission.[28] Copyright 2010, American Chemical Society.

interpretation. The bright dots in Figure 7a correspond to the Ce columns, while the O columns surrounded by four Ce columns are hardly visible because of the low atomic number of O. In

contrast, ABF-STEM images have a low scaling rate with the atomic number and have shown to be a robust technique for simultaneous imaging of light and heavy elements.[29] In Figure 7b the O columns appear with a grey contrast and are highlighted by the red arrows. Multislice HAADF and ABF image simulations are performed to support the interpretation of the experimental images. Ce columns were clearly observed even in the core region of the GBs, as marked by quadrilaterals in Figure 7d. However, their contrast, due to the presence of O columns inside the GB, is weaker than in the bulk, which is consistent with the fact that the density of O columns in the GB is half that in the bulk. EELS analysis confirms the presence of oxygen vacancies in the GB. The EELS spectrum from the GB region is slightly broader than that from the interior region, indicating the presence of Ce^{3+}. The M_5/M_4 intensity ratio at the GB also tends to be larger, pointing toward the presence of Ce^{3+} (Figure 7g). These results reveal that oxygen non-stoichiometry plays a critical role in the stable GB structure of CeO_2.

The same group extended their research also towards different GBs such as Σ9 [110]/{221}, Σ11 [110]/{332}, Σ13 [001]/{510}, Σ3 [110]/{111} and Σ5 [001]/{210}, theoretically predicted GBs models are overlaid in the right part of each STEM images.[30] It is obvious that the GB core structures are all different, but all the GBs are well bonded at an atomic scale without amorphous or secondary phases (Figure 8a-e). EELS spectra indicate that the valence state of Ce depends on the type of GB: Ce is partially reduced to +3 in Σ5, Σ11 and Σ13 GBs, however, the valence of Ce maintains +4 in Σ3 and Σ9 GBs (Figure 8f, g). These results suggest that oxygen vacancies are formed at Σ5, Σ11 and Σ13 GBs, while Σ3 and Σ9 GBs maintain their oxygen stoichiometry. By combining atomic scale STEM and density functional theory (DFT), a quantitative determination of the O vacancy concentration can be obtained for the different GBs. The results indicate that the oxygen-vacancy concentration of the non-stoichiometric Σ5 GB is higher than that of the Σ13 GB, followed by the Σ11 GB. These results highlight the power of advanced electron microscopy combined with theoretical calculations to determine

the detailed atomic structure GBs in CeO_2. Such results pave the way towards a deeper understanding of non-stoichiometry in nanostructures.

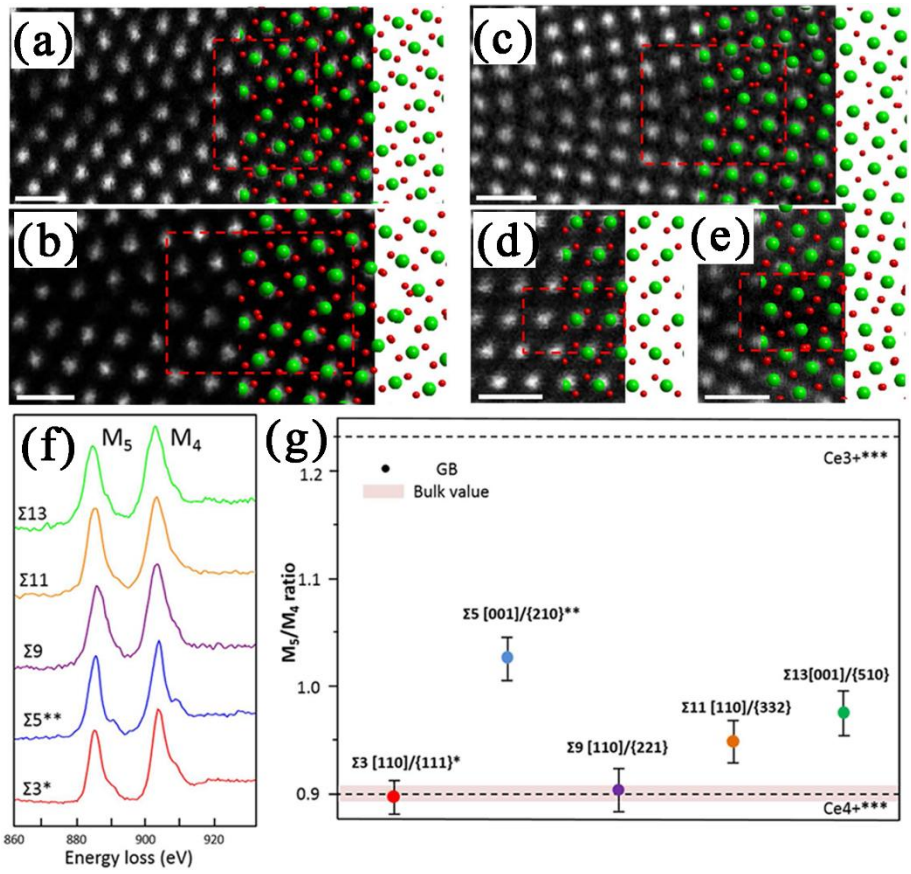

Figure 8 (a-e) HAADF-STEM images of five model GBs: (a) Σ9 GB, (b) Σ11 GB, (c) Σ13 GB, (d) Σ3 GB and (e) Σ5 GB. The bright dots correspond to Ce atomic columns. Theoretical GB models are overlaid in the right part of each image (green circles represent Ce). Note the good agreement between theoretical calculations and experimental images. Stoichiometric GB models are shown in (a, d), while non-stoichiometric GB models are used in (b, c, e). The red rectangular region in each image is the unit used for the EELS analysis. (f) Ce $M_{4,5}$ edge EELS spectra obtained from the area shown in (b). (g) The M_5/M_4 ratios calculated from the positive part of the second derivative of the spectra in (f). The pink area is the bulk value. Reproduced with permission.[30] Copyright 2016, Springer Nature.

3.6 Morphology effect

Extensive research has demonstrated that the morphology of a nanostructure profoundly affects its catalytic performance. Specifically, active sites can be tuned and enriched by controlling the morphology of nanocatalysts, which allows a selective exposure of highly active facets. This phenomenon is called morphology-dependent nanocatalysts.[2a, 2b, 17a, 31] A fundamental understanding of the active sites in morphologically controlled CeO_2 nanostructures, enclosed by the desired facets, is therefore important. It can provide a new strategy for the developing highly efficient nanocatalysts.

The morphology-dependent catalytic activity of CeO_2 was first described by Zhou et al.[32] They demonstrated that CeO_2 nanorods are more reactive for CO oxidation than irregular nanoparticles, even when these nanoparticles have a smaller size and a bigger Brunauer-Emmett-Teller (BET) surface area. HRTEM results reveal that CeO_2 rods predominantly expose well-defined {001} and {110} planes, whereas the more stable {111} planes are mainly found on CeO_2 nanoparticles. In the course of the reaction, CO extracts an O atom from a surface -Ce^{4+}-O- linkage, creating an oxygen vacancy. The redox features and the catalytic performance of CeO_2 nanowires, nanorods and nanoparticles were comparatively studied by Tana et al.[3a] In their study, CeO_2 nanowires present an even higher catalytic activity for CO oxidation and oxygen storage capacity than nanorods, although both of them are more reactive than the nanoparticles. Since CeO_2 nanowires/nanorods predominantly expose the reactive {110} and {100} planes, it is reasonable that the CeO_2 nanowires/nanorods have a higher efficiency. Considering the fact that vacancy formation energies follow the order (110) $<$ (100) $<$ (111) and that the reducibility of Ce is better on {100} surfaces, a direct correlation can be drawn between the morphology and the catalytic performance. A higher efficiency can be

obtained on controllable synthesized CeO_2 nanostructures with a large quantity of exposed {001}/{110} surfaces.[1f, 33]

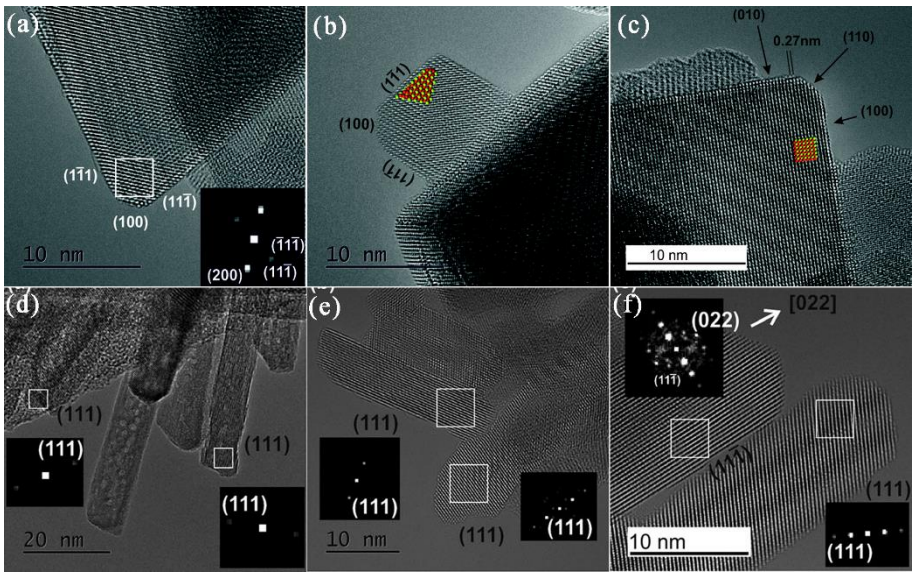

Figure 9 [011] *AC*-TEM images of large (a) and small (b) CeO_2 octahedra, exposing mainly {111}facets and very small {100}facets. The inset in (b) shows the structure of the CeO_2 lattice (Ce: green; O: red). (c) *AC*-TEM image of a cube nearly oriented along its [010] axis. The projected [010] structure is shown as inset. *AC*-TEM images of CeO_2 rods at two different magnifications [(d) and (e)]. Insets are FFTs of the boxed region. (f) The lattice fringes confirm that the surfaces are {111} and the growth direction is <110>. Reproduced with permission.[17a] Copyright 2013, Wiley.

Agarwal et al. dedicated themselves to the investigation of different CeO_2 nanostructures (octahedra, rods, and cubes) using advanced *AC*-TEM.[17a] Both for large and small octahedra, the prominent {111} facets show clearly resolved rows of Ce columns (Figure 9a and b). Figure 9c shows an atomic resolution image of a CeO_2 cube, mainly composed of {100} surfaces. CeO_2 nanorods grow along the [110] direction, in agreement with previous reports.[34] However, only {111} surfaces were found, without any {110} surfaces. Lattice resolution in the end-on view is difficult due to the length of the nanorods. They therefore suggested that the only

prominent well-defined facets are the {111}, while the other surfaces are irregular and not well defined (Figure 9d-f). These TEM observations help one to understand why the WGS catalytic efficiency of octahedra and nanorods are similar and why the cubes are more reactive.

3.7 Size effects and influence of defects

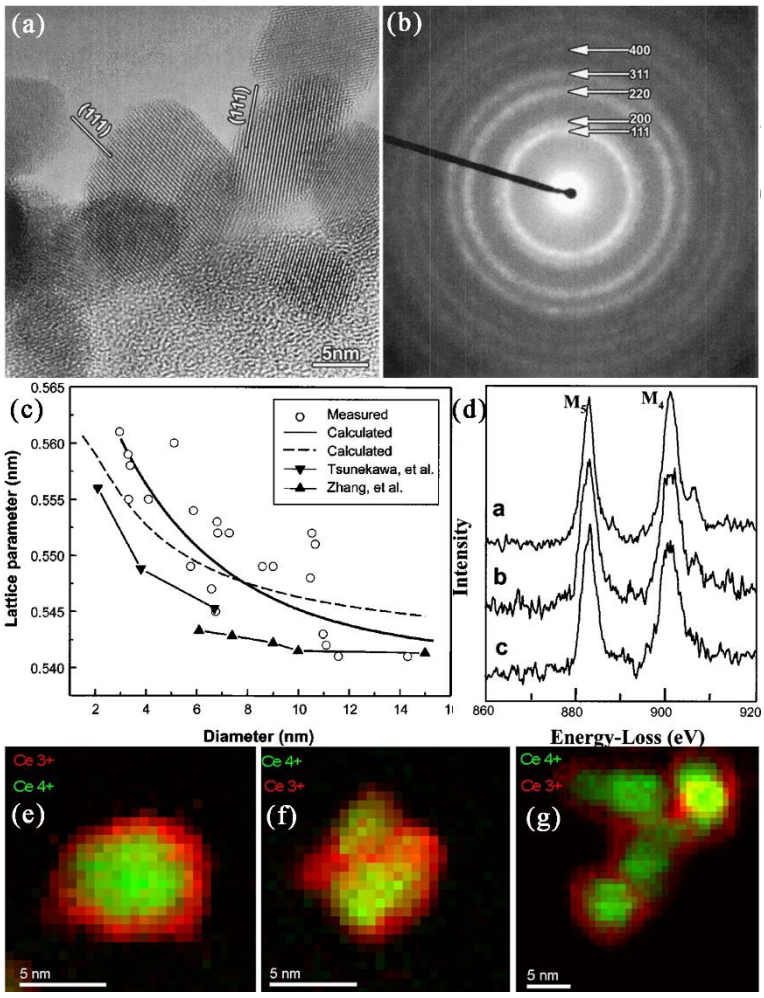

Figure 10 High resolution TEM image (a) and electron diffraction (b) of an assembly of CeO_2 particles. (c) Lattice parameter of the CeO_2 particles as a function of the particle size. (d) EELS spectra of different size nanoparticles. EELS maps of CeO_{2-x} nanoparticles of comparable size obtained by (e) post oxidation in the deposition chamber, (f) direct oxidation in the aggregation chamber, (g) oxidation in HV. Reproduced with permission.[35] Copyright 2004, American Physical Society; copyright 2016, IOP Publishing.

Another key parameter that can influence and modify the catalytic properties of CeO_2-based nanostructures is the particle size. Wu et al. investigated the crystal structure and valence change of CeO_2 for various sizes of particles using HRTEM, ED and EELS (Figure 10a-c).[35a] EELS enables an investigation on a single nanoparticle, overcoming the limitation of X-ray

photoelectron spectroscopy (XPS) which requires a large number of nanoparticles with unavoidably variations in size. The lattice parameters of CeO_2 increase with decreasing particle size (Figure 10c), as can be deduced from the SAED patterns. With varying particle size, also the EELS spectra are changing (Figure 10d). Ce^{4+} is only present for the larger particles (11 nm), while for the smaller particles (3.5 and 6 nm) the major contribution is from Ce^{3+}. This confirms that the reduction of Ce^{4+} to Ce^{3+} mainly takes place at or near the surface. Hailstone et al. extended this research by decreasing the size to 1 nm and registered a lattice expansion of almost 7%.[36] ED confirms the fluorite structure of CeO_2, without the presence of cubic or hexagonal Ce_2O_3. Their study also indicates that there is still some OSC even for a size down to 1 nm, which conflicts the proposal of Wu et al. who suggested that nanoparticles below 3 nm should be completely composed of Ce^{3+}. This discrepancy might be induced by the different synthesis methods in their work, but also a reduction under the electron beam in some of these researches may not be fully excluded.

The valence state of the CeO_2 nanotubes with different diameters has been studied by Han et al.[37] Also here, the intensity of the M_5 edge increases with a decrease of the diameter of the tubes, and the fraction of Ce^{3+} is estimated to be 0.90, 0.78, and 0.35 for d = 14.6, 17.3, and 25.5 nm, respectively. For the same diameter, the fraction of Ce^{3+} in the CeO_2 nanotubes is significantly larger than for CeO_2 nanoparticles, which may be due to the fact that there are two surfaces for nanotubes (inner and outer surfaces).

Spadaro et al. investigated the influence of structural defects by comparing three different sample preparations of CeO_2 nanoparticles (Figure 10e-g).[35b] The EELS results show that Ce^{3+} is mainly present on the surface for the post oxidized sample, forming a core-shell structure with a Ce^{4+} core (Figure 10e). Things are quite different for directly oxidized samples where Ce^{3+} is also detected near the core region (Figure 10f); this can be explained by assuming that small CeO_2 clusters with Ce^{3+} valence on the surface are formed first before they interact with

each other to coalesce into larger nanoparticles. The valence distribution for the sample oxidized in HV is similar to the post oxidized sample (Figure 10g). The Ce^{3+}/Ce^{4+} concentration decreases with increasing size of the nanoparticles, in agreement with previous reports.[14a, 38]

3.8 Growth mechanism

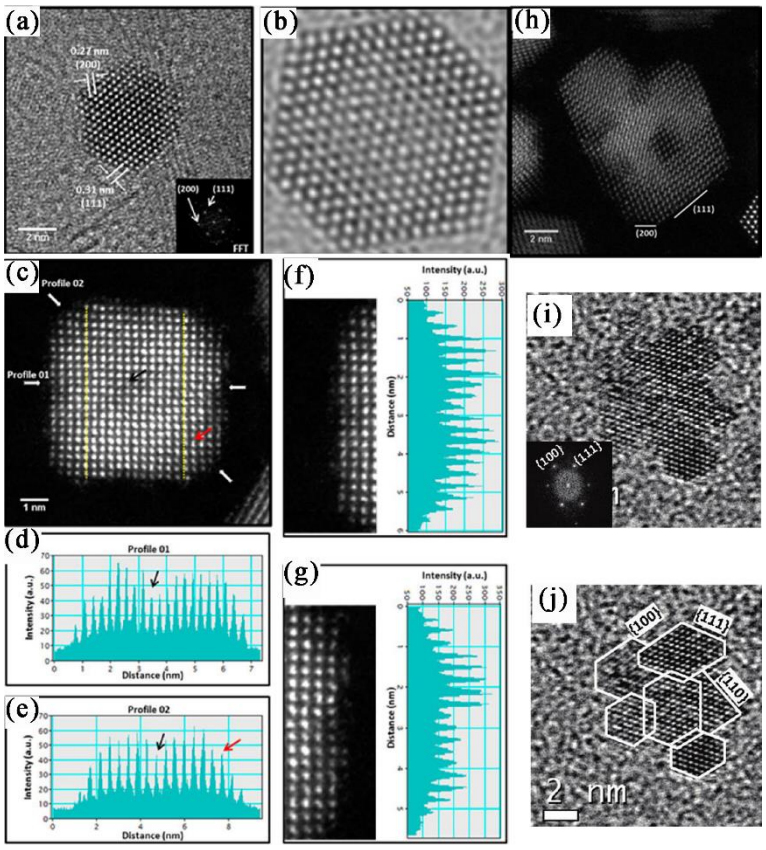

Figure 11 (a) HRTEM image together with its FFT and (b) simulated image oriented along the [110] zone axis for a low concentration of OLA. (c) HAADF-STEM image of a cube-like CeO_2 (high concentration of OLA) oriented along [001] with {200}, {220}, and {111} exposed facets. (d) and (e) intensity plot profiles along directions indicated by white arrows in part (c), and (f) and (g) intensity plot profiles along the left and right termination facets in (c); respectively. (h) STEM image of an isolated CeO_2 particle. (i) and (j) show a HRTEM image and the schematic outlines of the oriented aggregation of six CeO_2 nuclei. Reproduced with permission.[15a, 39] Copyright 2013 and 2012, American Chemical Society.

Crystal morphology is the result of a delicate balance between thermodynamic and kinetic processes during the growth process.[2c, 2d, 31b, 40] Indeed, various morphologies of CeO_2 nanostructures can be produced by different synthesis protocols and consequently different crystallographic planes can be exposed, which evidently affects the performance in widespread

applications. Through precisely control the experimental parameters such as temperature, concentration, pH value and organic additives, different morphologies of CeO_2 nanostructures can be obtained including nanocubes, nanowires, nanotubes and even hollow structures.[1a, 2c, 34, 41] Nevertheless, the evolution of the morphology and surface structure during the synthesis process is still not well understood.

An elegant example of demonstrating the growth mechanism of CeO_2 nanostructures was given by Cordeiro et al.[15a] At a low concentration of the stabilizing agent (OLA), a polyhedral CeO_2 with {200} and {111} surfaces was obtained, as shown in Figure 11a, b. Doubling the concentration of OLA leads to cube-like CeO_2 with a concave surface structure with {220} surfaces in addition to {200} and {111} surfaces (Figure 11c). The intensity drop in the central area of the cube-like CeO_2 is interpreted, according to image simulations, as about 5 Ce atoms missing in one column. A key mechanism for controlling the growth of nanostructures, was mainly found in the results at lower concentration of OLA.[42] In this sample, oriented linking between particles was mainly observed between {111} surfaces rather than {200} (Figure 11h), which can be explained by the higher surface energy of {200} surfaces with OLA. It is suggested that the growth process is not a simple evolution from a polyhedral to a cube-like nanostructure when changing the amount of stabilizing agent, but that it occurs via a more complex process. Similar phenomena were also observed by Lin et al. during the experiments with polyvinylpyrrolidone (PVP) as stabilizing agent.[39] An oriented attachment process of a number of small clusters, octahedral nuclei with exposed {111} and {100} surfaces and cubic ones with {110} and {100} surfaces (Figure 11i, j). PVP apparently prevents the agglomeration of nanoparticles in a hydrothermal reaction and gives rise to the growth of well dispersed and large nanoparticles through oriented attachment.

The formation mechanism of single-crystalline CeO_2 nanorods by self-assembly of CeO_2 nanoclusters was explored by Du et al.[43] The main shape of the ceria nanoclusters is the

truncated octahedron enclosed by {111} and {100} planes (Figure 12a, b).[34, 44] By prolonging the reaction time, CeO_2 nanorods are formed along the [211] or [110] direction by self-organization of truncated octahedral nanoclusters, sharing the {111} or {200} planes with each other (Figure 12c, d). CeO_2 nanorods with a [211] growth direction were also obtained in Ji's group (Figure 12e, f).[45] Generally two types of oriented attachment pathways can be identified: one is an alignment along the [211] direction with exposed {111} surfaces, the other one is along the [110] direction with exposed {200} surfaces. Considering the fact that the CeO_2 {111} surface is the most stable surface, a CeO_2 nanorod alignment along the [211] direction is only observed in this research.[22a] By increasing the reaction time the surface of the nanorods becomes much smoother, which suggests Ostwald ripening as the main process during the later stage of the reaction (Figure 12g).

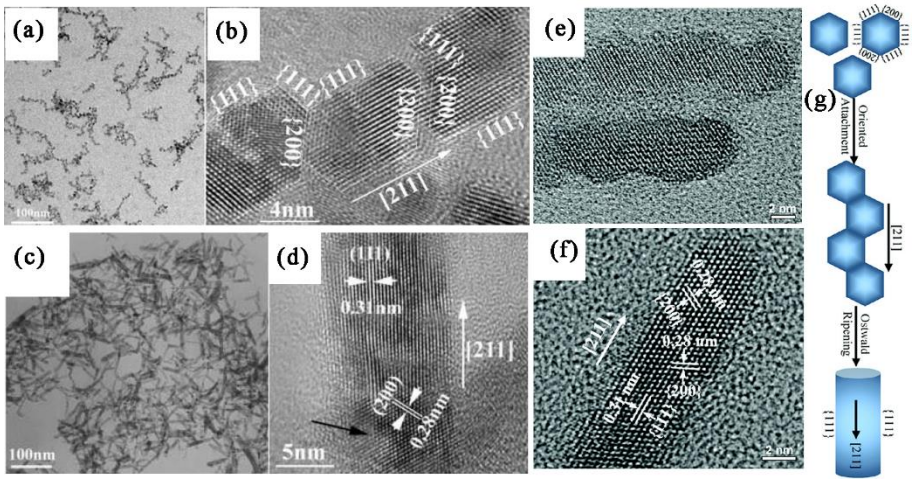

Figure 12 Low and High-magnification TEM images of nanoclusters (a, b) and nanorods (c, d). HRTEM images of CeO_2 nanorods obtained from a standard synthesis with 0.1 M $CeCl_3$ after (e) 8 h and (f) 15 h hydrothermal treatment at 220 °C. (g) Schematic diagram of the formation of CeO_2 nanorods along the [211] direction via oriented attachment followed by Ostwald ripening. Reproduced with permission.[43, 45] Copyright 2007 and 2012, American Chemical Society.

3.9 Composition effects

In addition to pure CeO_2 nanostructures, also CeO_2-based nanocomposites have attracted interest and have interesting applications. For instance, the CeO_2-ZrO_2 solid-solutions with a diameter in the nanometer range usually have high specific surface areas and high oxygen storage capacities, which highly improve the catalytic performance.[46] Introduction of other dopants, especially transition and rare earth elements, into the CeO_2 lattice can engineer active centres.[47] In order to maximize the catalytic performance and reduce the cost of noble metal nanoparticles, CeO_2 is often selected as support to provide a high surface area to stabilize small nanoparticles under a long-term catalysis process and at the same time provide a strong metal support interaction on the two-phase interface.[48]

3.9.1 Doping

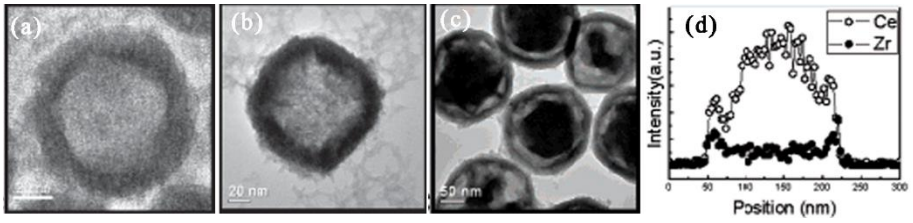

Figure 13 Representative TEM image of (a) spherical Ce-Zr-O Nanocages, (b) cubic-like Ce-Zr-O nanocages, (c) hollow core-shell Ce-Zr-O nanostructures. (d) Compositional line profile across a single hollow core-shell structure probed by EDS line scanning. Reproduced with permission.[46a] Copyright 2008, American Chemical Society.

By using colloidal CeO_2 nanoclusters as both precursors and templates, Wang et al. successfully fabricated well-defined $Ce_{1-x}Zr_xO_2$ and CeO_2@$Ce_{1-x}Zr_xO_2$ nanocages (Figure 13a-c) with different interior and exterior morphologies.[46a] TEM imaging suggests that the Kirkendall effect plays a critical role in the evolution of these nanostructures. A compositional line profile across a single CeO_2@$Ce_{1-x}Zr_xO_2$ acquired by EDX (Figure 13d) reveals that there

is more Zr in the outer shell than that in central area, which confirms that the shell is a $Ce_{1-x}Zr_xO_2$ solid solution while the core is mainly CeO_2. $Ce_{1-x}Zr_xO_2$ nanorods investigated by Chen et al. show that the ZrO_2 doping slightly decreases the diameter to about 8 nm, but remarkably shortens the length to about 40 nm.[49] TEM along different orientations demonstrates that the $Ce_{1-x}Zr_xO_2$ nanorods are enclosed by two (110) front planes, two (100) side planes and two (110) end planes.

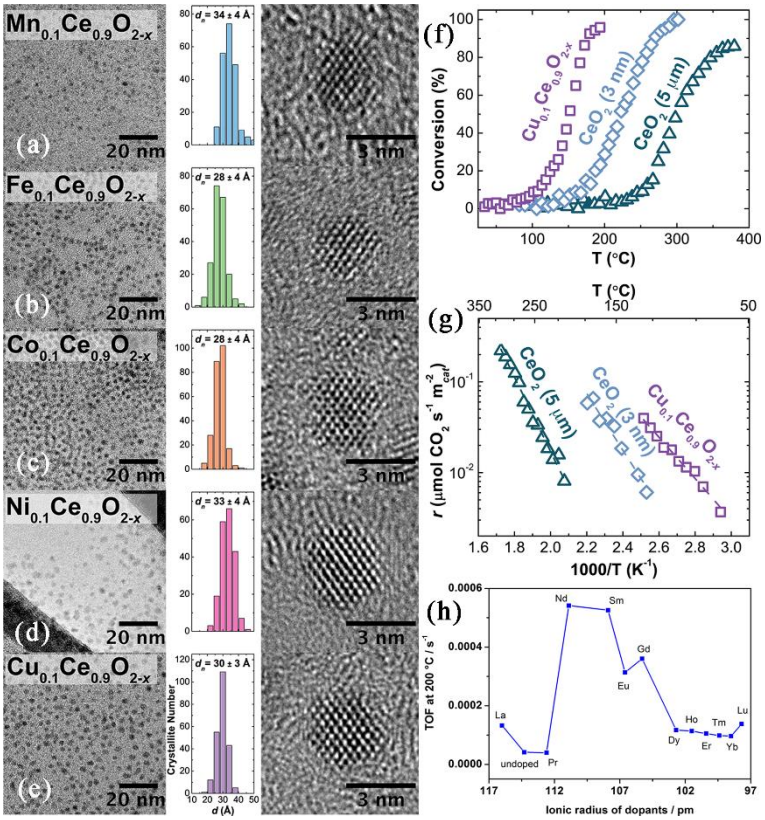

Figure 14 TEM image, histogram of particle size and HRTEM images of as-synthesized $M_{0.1}Ce_{0.9}O_{2-x}$, M = Mn (a), Fe (b), Co (c), Ni (d), Cu (e). CO oxidation catalysis on annealed 3 nm $Cu_{0.1}Ce_{0.9}O_{2-x}$, 3 nm CeO_2 and commercial 5 μm CeO_2 (Sigma-Aldrich); (f) light off curves and (g) area-normalized Arrhenius plots. (h) Catalytic activity for CO oxidation over CeO_2: Ln NWs and its relation to the ionic radius of the dopant. Pr-doped and undoped ceria were placed according to the ionic radius of their trivalent cations for comparison. Reproduced with permission.[47a, 47c] Copyright 2014 and 2013, American Chemical Society.

Transition-metal-substituted CeO_2 nanostructures ($M_{0.1}Ce_{0.9}O_{2-x}$, M = Mn, Fe, Co, Ni, Cu) have been systematically studied by Elias et al., demonstrating that the CO oxidation efficiency is greatly improved by incorporating Cu.[47a] TEM analysis confirms a narrow size distribution of 3.0 (±0.4) nm for $M_{0.1}Ce_{0.9}O_{2-x}$ (Figure 14a-e); the aliovalent transition metal atoms are successfully doped into the CeO_2 nanostructure maintaining a truncated octahedral morphology with {111} and {100} facets, providing superior catalytic efficiency (Figure 14f, g). EDS results indicate that the average transition metal concentration is between 8-14 mol%. Because of the similar valence and ionic radius of the lanthanide elements (Ln), Ke et al. also explored dopant-induced modifications of the catalytic activity in CeO_2: Ln (Ln = La−Lu) nanowires.[47c] EDS elemental mapping indicates that the distribution of the Ln (Ln = La−Lu) is uniform within the nanowires, showing good chemical homogeneity of the doped samples. The CO oxidation reactivity over CeO_2: Ln nanowires is dependent on the Ln dopant, and the reactivity reaches a maximum in turnover rate for Nd-doped samples (Figure 14h).

The local environment and the valence state of Fe and Ce in nanoscale Fe: CeO_{2-x} oxygen storage material can be investigated by *AC*-TEM combined with EELS before and after a model looping procedure, as shown in Figure 15.[25] EELS maps show that the Fe dopants are enriched at the surface the as well as in the voids of the CeO_2 nanoparticles. During the reduction/oxidation step at elevated temperature, oxygen vacancies in CeO_2 are mobile and cluster into elongated void structures. EELS maps also indicate that these voids have reduced Ce^{3+} walls and are Fe^{2+}-rich. After ten cycles under chemical looping conditions, the Fe in the Fe: CeO_{2-x} nanostructure starts to agglomerate and form small clusters at sintered CeO_2 grain boundaries (Figure 15b); the valence state is +2, as deduced from the EELS fine structure. The transfer of electrons and oxygen ions between Ce and Fe ensures a fast regeneration of available sites, which adds to the catalytic performance of Fe:CeO_{2-x}.

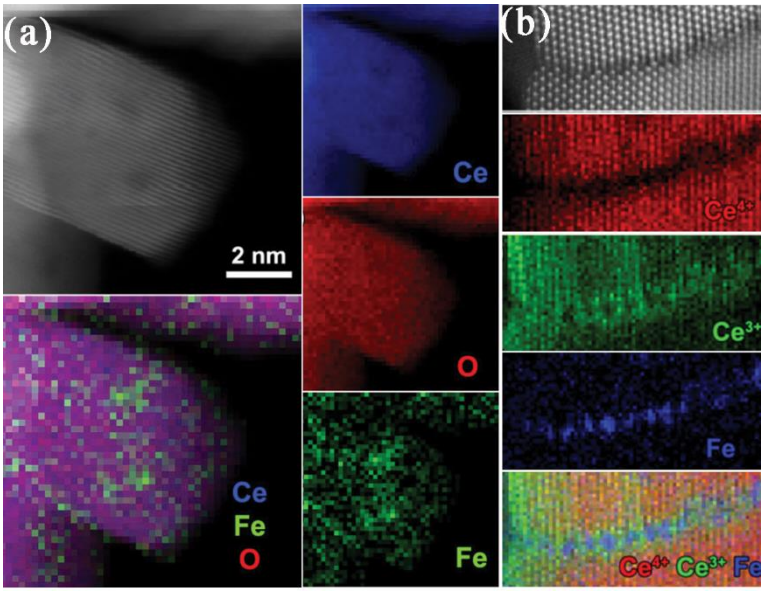

Figure 15 (a) Overview HAADF-STEM image together with elemental maps of Fe: CeO_{2-x}. (b) The high resolution STEM image together with elemental EELS maps for Ce^{4+}, Ce^{3+} and Fe after 10 redox cycles. Reproduced with permission.[25] Copyright 2015, Royal Society of Chemistry.

3.9.2 Mixed oxide interfaces

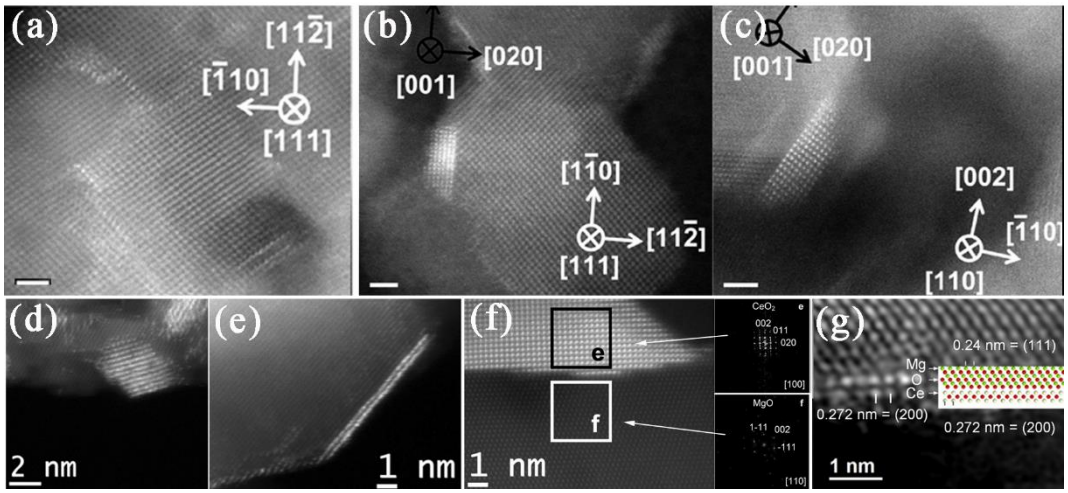

Figure 16 HAADF-STEM images showing the different morphologies of ceria: (a) ceria chains. (b, c) epitaxial ceria nanoparticles on titania. The Ce shows up with a brighter contrast because of its higher Z-number (58) compared to Ti (22). HAADF-STEM images of (d) a fresh CeO_2/MgO sample, (e) one CeO_x layer and (f) a CeO_2 nanoparticle deposited over MgO, and FFT of the CeO_2 nanoparticle and the underlying MgO support respectively. (g) HAADF-STEM image of the contact between a CeO_x bilayer and MgO. Reproduced with permission.[50] Copyright 2013, American Chemical Society; copyright 2015, Wiley.

The detailed nature of the mixed-oxide interface in TiO_2-CeO_2 nanostructures can be revealed using *AC*-TEM.[50a] HAADF-STEM images reveal that CeO_2 can demonstrate hierarchical structures with clusters, chains, and nanoparticles on a TiO_2 support (Figure 16a-c). The chain structures show a preferred growth habit along the TiO_2 [101] direction and the Ce atoms link to the Ti columns. The epitaxial orientation relationship between CeO_2 and TiO_2 is: (020) CeO_2||($\overline{1}\overline{1}$2)TiO_2 and [001]CeO_2||[111]TiO_2. In addition to dislocations, CeO_2 also contains high energy surface defects such as steps and kinks. STEM-EELS also allows to analyse the TiO_2-CeO_2 interface. The spatially overlapping chemical signatures of the Ti $L_{2,3}$- and Ce $M_{4,5}$-edges indicate that Ti diffuses into the CeO_2 nanoparticle, which is consistent with the fact that CeO_2 and TiO_2 can form solid solutions of the $Ce_{1-x}Ti_xO_2$ ($x < 0.2$) type.[51]

Also MgO is a relevant material that can be used as a support for catalytic reactions with advantages over TiO_2, such as its low price, its ability to stabilize and avoid sintering; moreover, its basic surfaces provide synergies with the acid surfaces of CeO_2.[52] Fresh CeO_2-MgO and the SRMO (Severe Reduction followed by Mild Oxidation) treated CeO_2-MgO have been studied in detail.[50b] In the fresh sample very bright dots on the MgO crystallites, corresponding to CeO_x are clearly detected, (Figure 16d). In the SRMO samples, CeO_x layers appear as bright thin lines, which cover some of the MgO facets. Figure 16e, g shows the contact between MgO and a CeO_x bilayer with $\{111\}_{MgO}$ parallel to $\{001\}_{CeO2}$. Larger CeO_2 nanoparticles on the MgO surface (Figure 16f) show an orientation relationship $[110]_{MgO} \parallel [001]_{CeO2}$. STEM-EELS spectra from different areas of the fresh CeO_2-MgO sample confirm that the isolated bright spots in the HAADF-STEM images are indeed Ce containing species. The fine structure of the Ce $M_{4,5}$ EELS line indicates that the structures at the grain boundaries are fully oxidized Ce +4, whereas those at the surface contain a mixture of oxidized +4 and reduced +3 Ce. The interface structure between the larger CeO_2 nanoparticles and the MgO support in the SRMO sample shows that the first row of Ce atoms in contact with the MgO is predominantly Ce^{4+} type, while those in the second row are a Ce^{3+}-rich mixture.

3.9.3 Metal-support (M)-CeO_2 interactions

Au-CeO_2

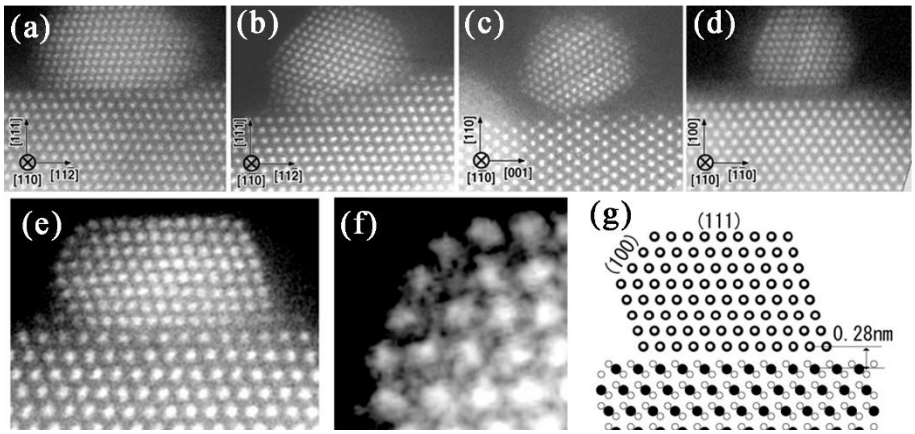

Figure 17 Profile-view HAADF-STEM images of Au particles on CeO_2 (111) (a), vicinal surface (b), (110) (c) and (100) (d). HAADF-STEM image of Au on CeO_2 (e) and enlarged image of the Au (100) surface (f) and schematic drawing of the model of a Au particle on CeO_2 (111) (g). Reproduced with permission.[53] Copyright 2010, Trans Tech Publications.

Because of the excellent catalytic performance of Au-CeO_2 nanostructures for various applications, detailed information on the size of the Au nanoparticles and the interface structure between Au and the CeO_2 support is crucial.[1e, 48a, 54] Understanding the growth mechanism of Au particles on a CeO_2 support is therefore of primary importance.[5b, 55] Akita et al. performed ex situ TEM characterizations of the changes of Au nanoparticles under heating at various temperatures both in air and in an hydrogen stream.[55d] The average diameter of the Au nanoparticles changes from 1.9 to 6.1 nm after heating in air. Because of Ostwald ripening, large Au nanoparticles grow at the expense of smaller one, in agreement with the in situ heating experiments of Au nanoparticles on CeO_2.[55a] However, the size of the Au nanoparticles does not increase with increasing the temperature in a hydrogen stream. Oxygen vacancies are probably created on the CeO_2 surface, as observed by scanning tunnelling microscopy (STM) in ultra-high vacuum conditions, and prevent the diffusion of Au atoms in a hydrogen

atmosphere, suppressing growth of the Au nanoparticles.[54, 56] Figure 17 shows HAADF-STEM images of Au nanoparticles on various CeO_2 surfaces, which reveal that the interface features are different depending on the kind of CeO_2 surface.[53] For a CeO_2 (111) surface, flat and wide interfaces are often observed and direct connections of Au columns and Ce columns are formed. In Figure 17c a polyhedral Au nanoparticle is attached to the edge of an atomic step of the CeO_2 (110) surface. A flat interface is formed between Au on CeO_2 (100), while the distance between the Au and the Ce layer is large (Figure 17d). Au nanoparticles often exhibit a reconstructed {100} surface (Figure 17e, f), excess atomic columns and disordered arrangements are observed in Figure 17f, in comparison with the model structure shown in Figure 17g. The distance between the Au layer and the Ce interface layer is about 0.28 nm (Figure 17g), suggesting that the oxygen layer is absent at the CeO_2-Au interface.[55b, 55c]

With atoms clearly resolved, the size, morphology, and atomic interface structure of the Au-CeO_2 nanocatalysts before and after the WGS reaction were systematically studied by Lin et al.[57] Figure 18a-d shows high-magnification HAADF-STEM images of as-prepared Au-CeO_2 nanorods and nanocubes. The growth direction of the CeO_2 nanorods is along <112> and the predominantly exposed facets are {111}. Only a small portion of the Au is found on {100} surfaces (labelled as Au III in Figure 18a), and the preferred interface relationship is Au (111) [$\bar{1}$ 10]||CeO_2(111) [$\bar{1}$ 10]. For CeO_2-Au nanocubes, approximately 20% are Au (111)[1 $\bar{2}$ 1]||CeO_2(001)[100] and the other 80% Au(111) [$\bar{1}$ 10]||CeO_2(001)[100]. The schematic 3D views are shown in Figure 18e, f. No significant change of the average size and morphology of the Au nanoparticles is observed after the WGS reaction of the Au-CeO_2 nanorods. However, the average size of the Au nanoparticles on CeO_2 nanocubes increases from approximately 3.0±1.0 nm to 3.8±1.2 nm. Moreover, the morphology of the Au nanoparticles is slightly different after the WGS reaction. Additional {111} facets are present near the Au-CeO_2 interface, as indicated in Figure 18h. These results indicate that the loss of

adhesion of Au to the support CeO_2 is partly responsible for the decrease of the activity in a WGS reaction.

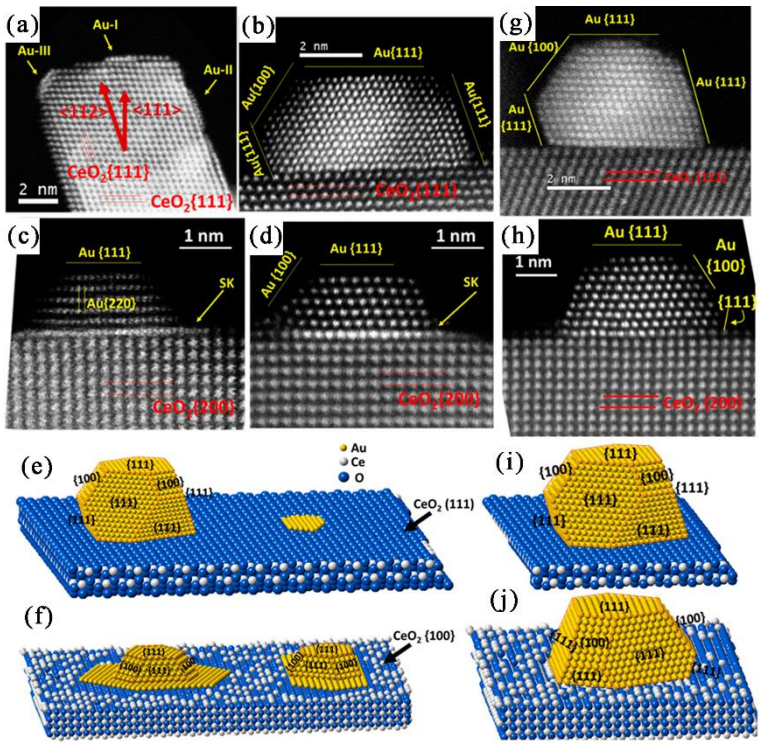

Figure 18 Morphology and atomic structure of Au-CeO_2 nanostructures before the WGS reaction, HAADF-STEM images of Au-CeO_2 nanorods (a, b) and Au-CeO_2 nanocubes (c, d). Schematic view of an Au particle and raft supported by the CeO_2 (111) surface (e) and the (100) surface (f). Morphology and atomic configuration of Au-CeO_2 nanostructures after the WGS reaction, HAADF-STEM image of an Au particle supported by a CeO_2 nanorod (g) and a CeO_2 nanocube (h). Schematic view of an Au particle supported by the CeO_2 (111) surface (k) and the (100) surface (l) after the WGS reaction. Reproduced with permission.[57] Copyright 2015, American Chemical Society.

Pt-CeO₂

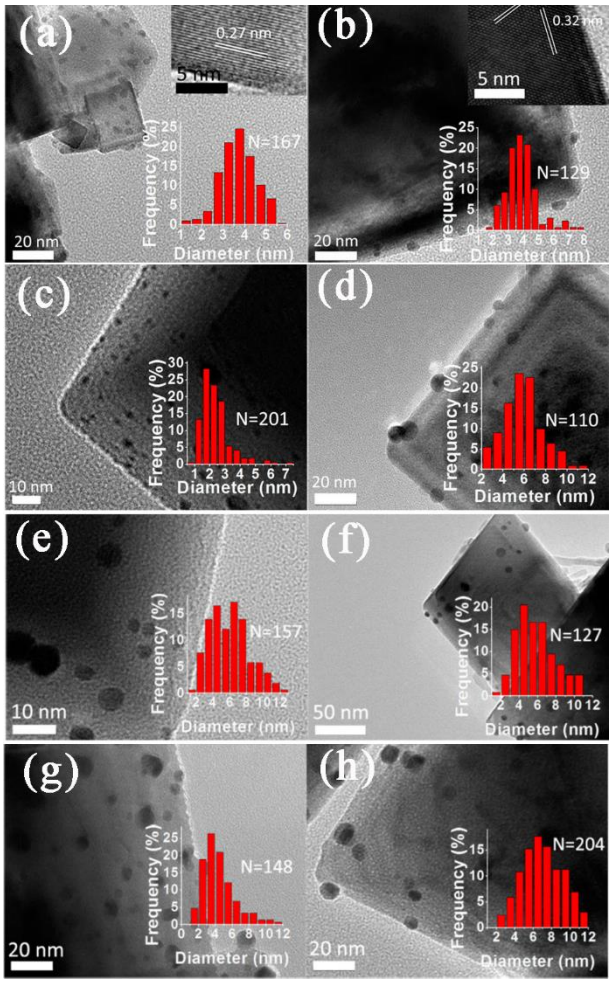

Figure 19 TEM images and Pt particle size distribution (a) Pt/cubes-as-received. (b) Pt/octahedra-as-received. (c) Pt/cubes-O20H30. (d) Pt/octahedra-O20H30. (e) Pt/cubes oxidized 20%O_2/N_2. (f) Pt/octahedral oxidized 20%O_2/N_2. (g) Pt/cubes reduced 5% H_2/Ar. and (h) Pt/octahedral reduced 5% H_2/Ar. Reproduced with permission.[58] Copyright 2014, American Chemical Society.

Pt-CeO_2 is another important catalyst for various catalytic reactions.[48b, 59] Redispersion of Pt nanoparticles on CeO_2 is an important route for catalyst regeneration and antisintering. Wu et al. systematically investigated the redispersion of Pt on CeO_2 nanoparticles with well defined surface planes including cube {100} and octahedral {111} planes (Figure 19).[58] After heat treatment in an alternating atmosphere of 20% O_2/N_2 for 20 s and 5% H_2/Ar for 30 s for a total

of 30 min (-O20H30), the average size of Pt on CeO_2 cubes decreases from 3.7 to 2.4 nm but increases from 3.9 to 5.9 nm on CeO_2 octahedral planes, (Figure 19 c, d). When treated in single oxidation atmosphere (20% O_2/N_2) for 30 min, the average size of Pt increases to 6.0 and 5.8 nm for Pt/CeO_2 cubes and Pt/CeO_2 octahedra respectively, while the average size of Pt becomes 4.6 and 7.0 nm for Pt/CeO_2 cubes and Pt/CeO_2 octahedra in a reduction atmosphere (5% H_2/Ar). These results indicate that the Pt size on Pt/CeO_2 octahedra grows in all three atmospheres, and Pt on Pt/CeO_2 cubes redisperses only in an alternating atmosphere while growing in a single reduction or oxidation atmosphere.

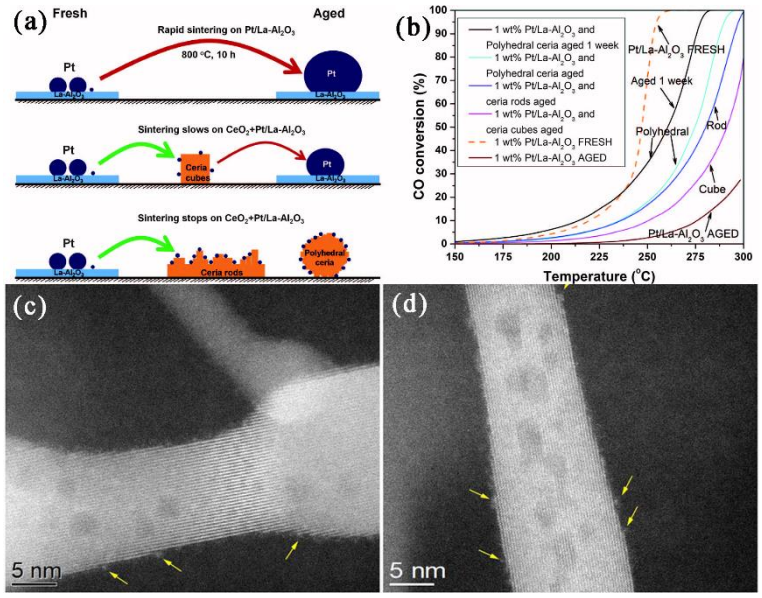

Figure 20 (a) Illustration of Pt nanoparticle sintering, showing how ceria can trap the mobile Pt to suppress sintering. Cubes appear to be less effective than rods or polyhedral ceria. (b) Light-off curves for CO oxidation on the 1 wt% Pt/La-Al_2O_3 sample (20 mg of catalyst in the reactor) and the samples physically mixed with ceria (20 mg of 1 wt % Pt/La-Al_2O_3 mixed with 10 mg of ceria powder) and then aged at 800°C in air. HAADF-STEM images of Pt/ceria rods treated at 800°C in flowing air for 10 hours after three cycles of CO oxidation (c, d) to 300°C, showing that the catalyst is stable after reaction and the Pt species remain atomically dispersed. The arrows point to step edges that appear to be sites where the Pt species are present, rather

than the smooth well-defined (111) facets. Reproduced with permission.[60] Copyright 2016, AAAS.

By varying the type of nanoparticle or reducing the size, the catalytic activity can eventually be enhanced and the cost reduced. However, smaller noble nanoparticles tend to coarsen during the catalytic reaction as a consequence of their high surface energy, especially for single atom catalysts.[61] To surmount this obstacle, tremendous efforts have been devoted to develop sinter-resistant, atomically dispersed nanocatalysts. By using CeO_2 nanoparticles with different morphologies and *AC*-TEM as a characterisation technique, Jones et al. determined the most effective surface for trapping Pt to prepare thermally stable single-atom Pt on CeO_2 nanocatalysts (Figure 20).[60] After aging the mixture of 1 wt% Pt/La-Al_2O_3 and CeO_2 in a weight ratio of 2:1 in flowing air, no Pt is present on the Al_2O_3; it has migrated to the CeO_2 phase and is trapped there, forming subnanometer Pt species. Even after three cycles of CO oxidation up to 300°C, some of the Pt on the CeO_2 rod is still atomically dispersed (Figure 20 c, d). These results on trapping of Pt atoms provide a plausible explanation for the role of CeO_2 in slowing down the rate of catalyst sintering and may guide the development for preparing single-atom catalysts.

The interface between CeO_2 epitaxial films and the (111) Pt surface is also studied by a combination of *AC*-STEM and ab initio density functional theory.[62] A statistical analysis of the size of the coincidence cells indicates that the registering locally changes from 3:4 to 2:3 and 5:7 without a preferential coincidence cell size (Figure 21a). An interfacial layer with the periodicity of the Pt substrate and having a much lower contrast can be identified in the red rectangle in Fig. 21a. A good contrast agreement is obtained assuming that the interfacial layer contains both CeO_2 and Pt in roughly the same proportion (Figure 21b). The Ce oxidation state at different distances from the interface can be obtained by collecting STEM-EELS spectra at the Ce $M_{4,5}$ edge; it indicates a non-negligible Ce^{3+} concentration of 15% ± 4% at the interface.

Compared with the bulk (blue line), the EELS spectrum of the interface (red line) is clearly shifted towards lower energy loss and has a higher M_5/M_4 branching ratio, as expected when the contribution from Ce^{3+} has a more relevant weight (Figure 21c).

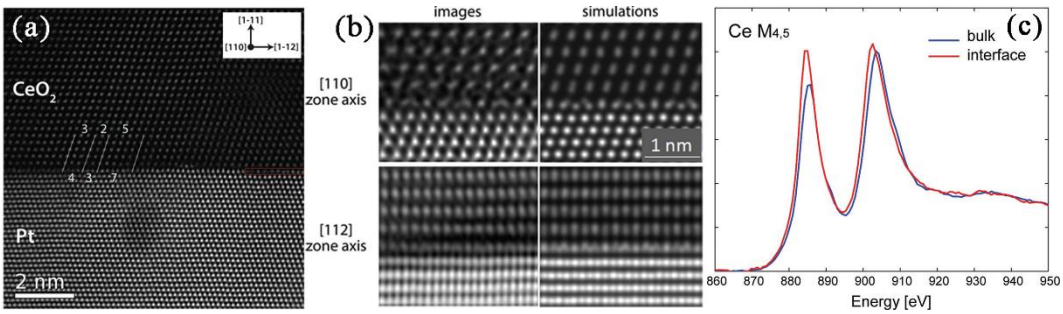

Figure 21 (a) Cross section HAADF-STEM of the CeO_2/Pt(111) interface imaged along [110]. The blue lines indicate the interface coincidence registry that varies locally from 3:4 to 2:3 and 5:7. The red rectangle indicates an interfacial region with the periodicity of Pt atomic rows and a lower contrast, comparable to the one in the CeO_2 layer. (b) Cross section HAADF-STEM images of the CeO_2/Pt(111) interface along the [110] and [112] zone axis together with the simulated images, obtained using the atomic positions of the model after structural relaxation. An interfacial layer with the same periodicity as Pt and a much lower contrast can be identified. (c) Ce $M_{4,5}$ edge spectra acquired at the interface (red line) and in the CeO_2 film bulk (blue line). Reproduced with permission.[62] Copyright 2015, Wiley.

Other M-CeO_2 nanostructures

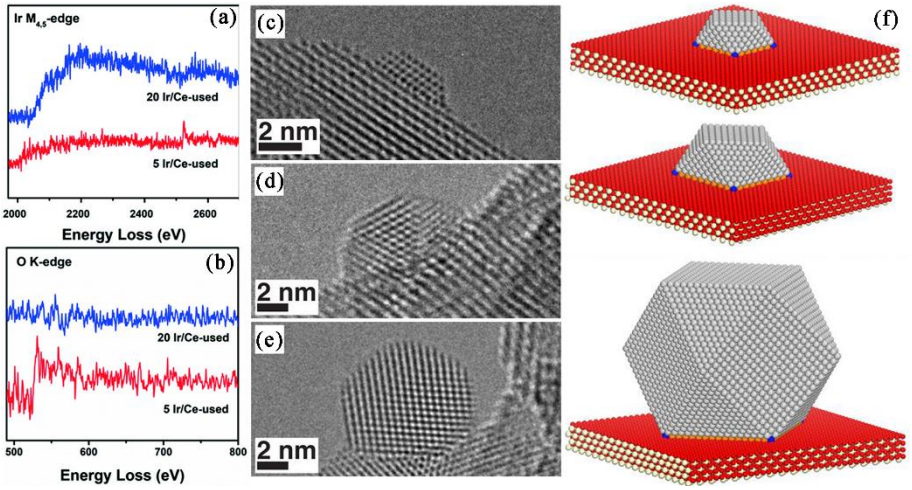

Figure 22 EELS of 5Ir/Ce-used (a) and 20Ir/Ce-used (b) catalysts. HRTEM images of Pd/CeO_2 catalysts after calcination at 300°C and reduction at 150°C: small (c), medium (d), and large (e) particles. (f) Physical models prepared to describe the particles. Blue, orange, and gray colors indicate corner, perimeter, and surface atoms, respectively; red and white are oxygen and cerium atoms of the ceria support. Reproduced with permission.[63] Copyright 2017, Wiley; copyright 2013, AAAS.

The importance of the dispersion and chemical structure of Ir species on CeO_2 nanostructures in the selectivity of the CO_2 hydrogenation has been demonstrated by Li et al.[63a] The average size of the Ir nanoparticles is 1.0 nm for 5Ir/Ce-used, 1.6 nm for 15Ir/Ce-used, and 2.2 nm for 20Ir/Ce (weight percent). No obvious aggregation or sintering of Ir nanoparticles has been found after the reduction and CO_2 hydrogenation reactions; this is related to the strong interaction between the support and the active species that stabilize the Ir particles. In order to provide evidence for the incorporation of O atoms in the Ir nanoparticles, STEM-EELS was used to directly collect both the Ir and O signal from Ir nanoparticles detached from the CeO_2 support (Figure 22a, b). The results suggest that a large number of O atoms are bound to the Ir species for the 5Ir/Ce-used catalyst, while the Ir particles are oxygen-free and metallic in nature

for the 20Ir/Ce-used catalyst. Because of the strong metal-support interactions (SMSI), O atoms are easier to be incorporated into the metal surface when decreasing the nanoparticle size, thus, smaller Ir nanoparticles have more under-coordinated atoms with higher catalytic efficiency. These results suggest that CeO_2 plays a key role in engineering the chemical properties of the supported Ir nanoparticles.

Using monodispersed, size-tunable metal nanoparticles, Cargnello et al. studied the role of the metal-support interface.[63b] Their results indicate that larger Pd nanoparticles maintain their original cuboctahedral morphology (Figure 22c-f), while the smaller ones spread over both supports into shapes that resemble a cubooctahedron truncated along the {100} direction. By using monodispersed Ni, Pd, and Pt nanocrystals with different size, the relative fraction of interfacial sites was varied on the CeO_2 support. Based on the turnover frequency (TOF) values of the CeO_2-based nanostructures, the perimeter metal atoms at the nexus of the metal, support, and atmosphere are suggested to be the active sites for catalysis reaction and that the larger surface-to-volume ratio of small nanoparticles translated to an increased boundary length and higher catalytic performance.

4. In Situ Transmission Electron Microscopy

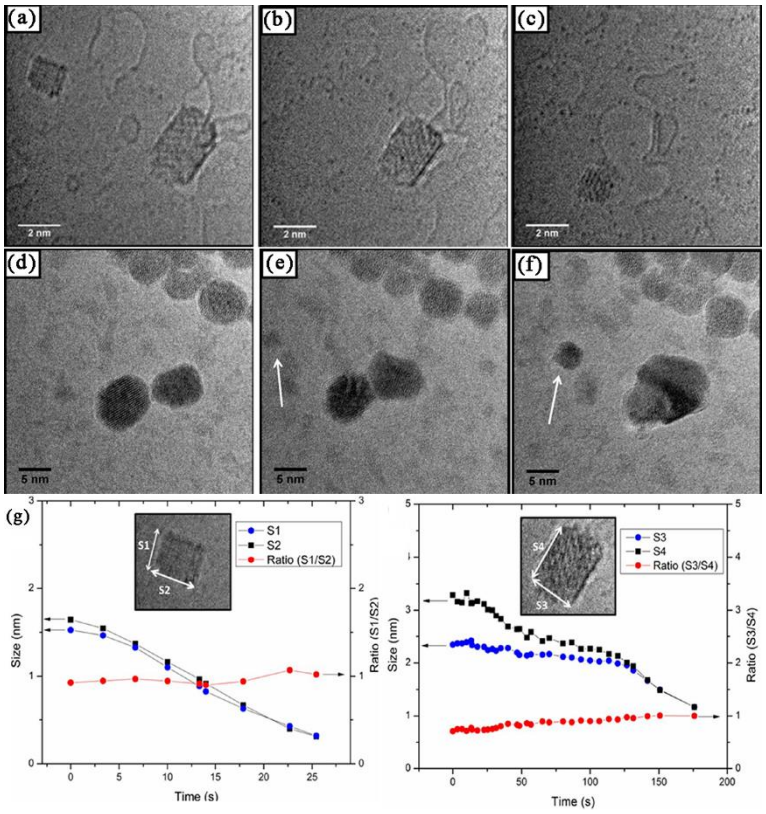

Figure 23 TEM images of CeO_2 nanocrystal dissolution during the experiment: (a) 0 s. (b) 64 s. (c) 220 s. A set of time-resolved images of an in situ TEM experiment with CeO_2 nanocrystals (vacuum, 890 °C), (d) 3 min. (e) 7 min. (f) 14 min. The white arrows indicate the formation of a new nanocrystal. (g) CeO_2 side size and the side ratio evolution for a small (left) and a larger nanocrystal (right). Reproduced with permission.[64] Copyright 2012, American Chemical Society.

Even though TEM/STEM has become a powerful tool for the characterization of nanostructures, traditional TEM/STEM can only record indirect phenomena, i.e. the reaction process as deduced by comparison of the nanostructure before and after reaction.[14a, 16, 60] Such process is unable to follow a complete reaction on the same nanostructure.[4a, 65] Moreover, most of the chemical reactions take place under dynamical conditions, such as high temperature, gas circulation, potential, liquid phase. Structure characterization via a post-mortem approach

may not represent the truly active sites emerging during the reaction.[4a, 8c, 66] Therefore, direct observations under operating conditions are of utmost importance. In-situ TEM, a method that broadly refers to real-time observations of nanostructures during exposure to an external stimulus such as temperature, gas or liquid environment, tensile strain, electrical or magnetic field, has frequently been used to study catalytic reactions.[4a, 66c]

4.1 In situ heating

The instability of CeO_2 nanoparticles seriously hindered the development of novel nanocatalysts. Valuable information on the thermal stability of CeO_2-based nanostructures can be obtained by in situ TEM experiments. Cordeiro et al. studied the thermal behaviour of CeO_2 nanoparticles by in situ heating up to 890 °C (Figure 23).[64] Smaller CeO_2 nanocrystals vanish in 30 s, while the larger CeO_2 nanocrystals disappear after about 240 s. The facets shrink homogeneously for the smaller; i.e. the facet size ratio (S1/S2) remains nearly constant. However, for the larger ones, the facet (S3) decreases more slowly than the larger facet (S4). They also noted a motion of particles during the ripening process as well as the coalescence and sintering of nanocrystals. These novel data on mass transfer at higher temperatures for CeO_2 nanoparticles will have an impact on the ripening models for explaining the thermal (in)stability.

4.2 Electrically driven redox process

Dynamic changes taking place during the electrically driven redox reaction of a CeO_2 film were recently explored using in situ TEM (Figure 24).[67] By increasing the bias to 6 V, a structural change takes place with the appearance of a wavy structure in the HRTEM image, (Figure 24b). At the same time, extra diffraction spots are observed under the applied electrical field, suggesting that oxygen anions have been removed from the CeO_2 film and that oxygen vacancies are structurally ordered as in Ce_2O_3. The structure model is displayed in Figure 24d.

EELS analysis confirmed the reduction and oxidation process of the CeO_2 film (Figure 24e). In situ TEM observations suggest that the reversible phase transformation is due to the migration of oxygen vacancies. These results could lead to a low-temperature operation for CeO_2 nanocatalysts by means of an electric field for applications such as solid oxide fuel cells, oxygen generation, solid state electrolytes, as well as catalytic reforming.

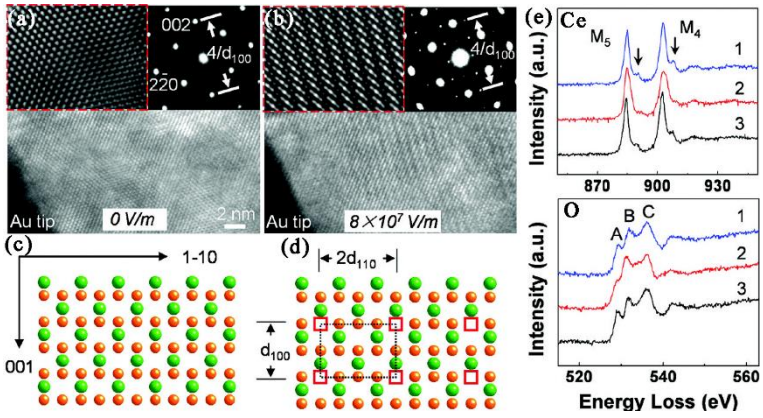

Figure 24 (a) In situ TEM image of a single-crystal CeO_2 film along the <110> zone axis. The enlarged HRTEM image and the corresponding SAED pattern are shown in the upper left and the upper right inset, respectively. (b) A wave-sweeping pattern appears when a bias of 6 V is applied across the CeO_2 film, indicating the decomposition of the cerium oxide. Superlattice reflections (upper left) and extra diffraction spots (upper right) were observed. (c) Model of CeO_2 in a perfect fluorite structure. (d) Solid-sphere model showing the formation of oxygen vacancies. The rectangles outlines the vacancy superlattice. (e) EELS spectra of the Ce-M edge and O-K edge. Spectra 1, 2, 3 were taken from the original CeO_2 film, after applying the electrical field, and after removing the electrical field, respectively. Reproduced with permission.[67] Copyright 2010, American Chemical Society.

4.3 In situ environmental TEM

4.3.1 CeO_2 and Ce-Zr solid solutions

Using environmental TEM (ETEM), one is able to study in situ atomic scale redox processes in individual CeO_2 nanoparticles (Figure 25a-i), which is a fundamental step to understand the redox functionality of CeO_2-based nanostructures in real catalytic applications.[68] Under 0.5 Torr of dry H_2 environment, a phase transformation takes place when increasing the temperature from 245 °C to 693 °C, resulting in the formation of a superlattice in which the (220) interplanar spacing of fluorite is quadrupled. Upon cooling down to 600 °C, these superstructure spots disappear rapidly. On the EELS spectra (Figure 25d-f), significant changes in the relative intensity ratio of the Ce M_5 and M_4 peaks are observed at 693 °C, indicating that most of the Ce has undergone a reduction to the +3 oxidation state. After heating the CeO_2 (110) surface in 0.5 Torr of H_2 for 30 min at 730 °C, the surface displays a gradual reduction in roughness with the elimination of saw-tooth points and the formation of a smooth profile compared with the surface at 266 °C.[69] After cooling for 1 h at 600 °C the surface is still flat and smooth, predominantly composed of (110) terraces with very little (111) component. This approach allows one not only to study the phase transformations within the nanoparticles, but also to explore surface transformations which may have an impact on the catalytic performance.

Also in the ceria-zirconia system, the redox activity of individual nanoparticles and the correlation with structure and composition has been explored by ETEM.[46b, 69] Analysis of Ce $M_{4,5}$ EELS white line intensity ratio indicates that one particle (Figure 25k) was more strongly reduced than the other (Figure 25j).[46b] A comparison of the reduction behaviour of these two nanoparticles as a function of temperature confirmed the higher activity in one nanoparticle because its valence state changed from +4 to +3, while a negligible change was found for a stable and relatively inactive nanoparticle. The most active nanoparticle has the lowest Ce concentration and a predominant fluorite structure without oxygen-vacancy ordering. Therefore, ETEM provides an exciting opportunity to isolate and identify phases with a different redox activity.

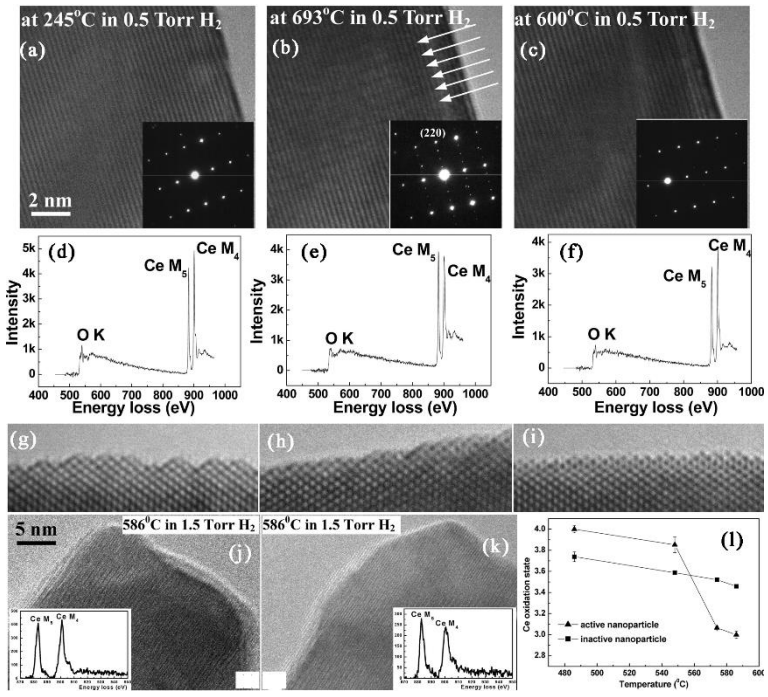

Figure 25 Dynamic structural changes characterized by HRTEM, electron diffraction and EELS at (a, d) 245 °C, (b, e) 693 °C, and (c, f) 600 °C in 0.5 Torr of H_2. After reduction, arrows in the high-resolution image (b) and extra spots along the [220]* direction in the electron diffraction pattern evidence the superstructure formed during reduction. A reversal of the Ce M_5/M_4 intensity indicates a reduction and re-oxidation from Ce^{4+} to Ce^{3+} and from Ce^{3+} to Ce^{4+} during heating and cooling, respectively. In situ profile images show the evolution of an identical region of a (110) surface of ceria during heating in 0.5 Torr of H_2 recorded at (g) 270 °C, (h) 730 °C and (i) 600 °C. In situ HRTEM images (j) and (k) from nominally identical ceria zirconia nanoparticles recorded at 586 °C in 1.5 Torr of H_2. The in situ EELS (inserts) show that the particle on the right is more strongly reduced than the particle on the left. (l) Oxidation state for the same two particles as a function of temperature. Reproduced with permission.[46b, 68-69] Copyright 2008 and 2009, American Chemical Society; copyright 2008, Elsevier.

4.3.2 Metal-support (M-CeO_2) interactions

Au-CeO_2

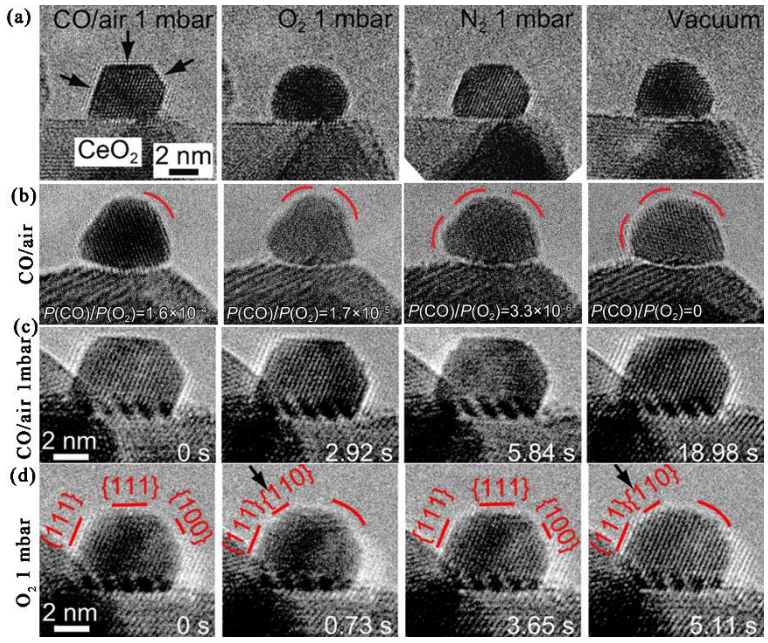

Figure 26 (a) Typical morphology of Au in various environments. (b) Morphology change of Au with a decrease of the partial pressure of CO in CO/air mixtures with total pressure 3 mbar. Frames from in situ ETEM observations of Au, during CO oxidation in (c) 1 vol% CO/air (1 mbar), and (d) O_2 (1 mbar). Reproduced with permission.[70] Copyright 2011, Wiley.

ETEM can also be used to study the morphology changes of Au nanoparticles supported on CeO_2 during CO oxidation.[70] In a 1 vol% CO/air gas mixture (1 vol% CO, 21 vol% O_2, 78 vol% N_2) at 1 mbar pressure, the Au appears to be a faceted polyhedron enclosed by the major {111} and {100} facets, as displayed in Figure 26a. The Au becomes rounded in pure O_2 gas, while Au exhibits major facets in both inactive N_2 gas at 1 mbar and in vacuum. The Au first becomes partly rounded when decreasing the CO pressure (Figure 26b), then the Au appears fully rounded once completely removing the CO. Obviously, these in situ observations prove that CO molecules stabilize the major {111} and {100} facets of Au. In CO-rich gas, the major facets were much more stable, while in O_2 gas, the minority {110} facets emerge frequently in

addition to the major {111} and {100} facets (Figure 26c, d). A restructuring of Au can be revealed at atomic resolution.[71] Under high vacuum, the interplanar distance between the topmost and second topmost surface layer is 0.20 nm, the interplanar distance along the <100> direction remains unchanged. The distance of Au atomic columns on the topmost layer is 0.29 nm, corresponding to the distance in a {100} plane of bulk Au, as shown in Figure 27a. However, the Au atom columns on the topmost and second topmost {100} layers shift to positions they do not normally occupy on a clean surface, both the average distance of the interplanar distance and the adjoining Au atomic columns changed to 0.25 nm, when introducing 1 vol % CO in air at 45 Pa at room temperature (Figure 27b). These experimental results provide a clue toward elucidation of the peculiar catalytic mechanism of supported Au.

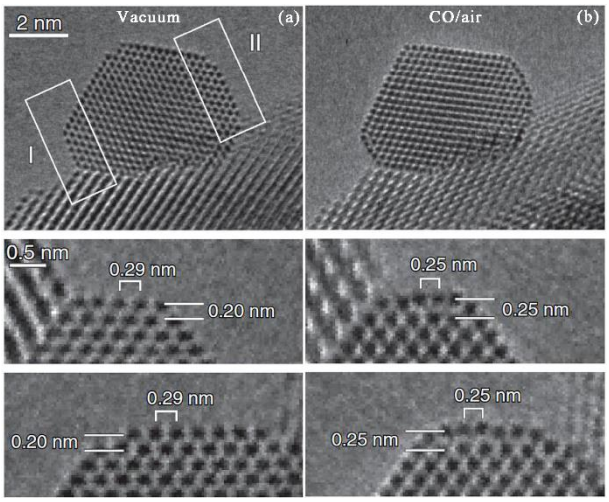

Figure 27 ETEM images of Au supported on CeO_2 in (a) a vacuum and (b) a reaction environment (1 volume% CO in air gas mixture at 45 Pa at room temperature). Regions I and II indicate two (100) facets. Enlarged images of these regions in vacuum and in the CO in air gas mixture are shown at the bottom of (a) and (b), respectively. Reproduced with permission.[71] Copyright 2012, AAAS.

The catalytic performance of Au is clearly affected by its electronic state which strongly depends on the contact interface with the support. The restructuring of the active Au-CeO_2

interface was explored by Ta et al.[72] Under an oxidizing environment (10 vol% O_2/N_2), the Au-CeO_2 interfaces retain their original configuration without noticeable variation in shape or size along with a rotation of the Au nanoparticles. However, Au-CeO_2 interfaces reconstruct with the appearance of disordered CeO_2 layers adjacent to the Au nanoparticles, under a reducing but reactive environment (42vol% CO/6vol% O_2/N_2) (Figure 28a). Kuwauchi et al. recorded the stepwise displacement of active Au nanoparticles on CeO_2, with the aim to clarify the atomic structures at the interface.[73] The location of the coincident atomic column changes with time, and finally returns to its initial position, indicating that the Au nanoparticles and the support CeO_2 are "mutually" displaced. Simulations of the interface models are consistent with the observations (Figure 28b). Meanwhile, rigid-body like rotations of Au nanoparticles, without lateral displacement, were also observed. No lateral displacement was detected, strongly indicating that the Au simply rotates about its axis normal to the interface. These in situ *AC*-ETEM observations provide direct experimental evidence of the dynamics at the interface of Au-CeO_2 nanostructures, suggesting that the most probable active sites are not structurally rigid.

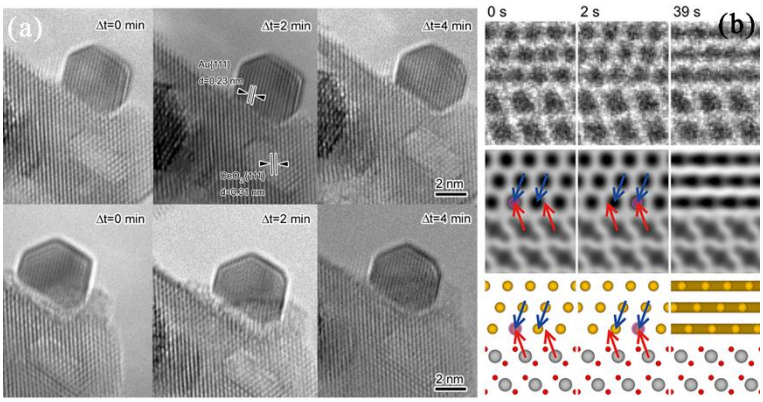

Fig. 28 (a) ETEM images of truncated octahedral Au under a 10 vol% O_2/N_2 environment (top) and a 42 vol% CO/6vol% O_2/N_2 atmosphere (bottom). (b) Observed images, corresponding simulated images, and modes for the interface are shown in the top, middle, and bottom rows, respectively. Atomic planes of gold and those of cerium are designated by blue and red arrows,

respectively. Reproduced with permission.[72-73] Copyright 2012 and 2013, American Chemical Society.

Pd-CeO_2

The modular Pd@CeO_2 nanosystem undergoes a structural evolution over a wide temperature range.[74] At 500 °C, a relatively small particle (solid and dashed yellow arrows in Figure 29) begins to dissociate into a 'cloud' of atomic-scale species, followed by the dissociation of three or more non-overlapping particles, indicated by the circles in the images at 10 and 22 min (Figure 29a). By increasing the temperature to 650 °C, a truncated octahedron bound by eight {111} planes and six {100} planes forms first, then, two crystallites coalesce, driven by the tendency to lower the overall surface energy. Meanwhile, very small (1-2 nm) features remain throughout the sample, similar to those observed in samples after ex situ calcination at 800 °C (Figure 29b). These in situ observations performed in an atmospheric gas cell at different temperatures provide real-time evidence that the Pd and CeO_2 nanoparticle in a dynamical process, which may open new perspectives about the origin of the activity of this nanocatalyst.

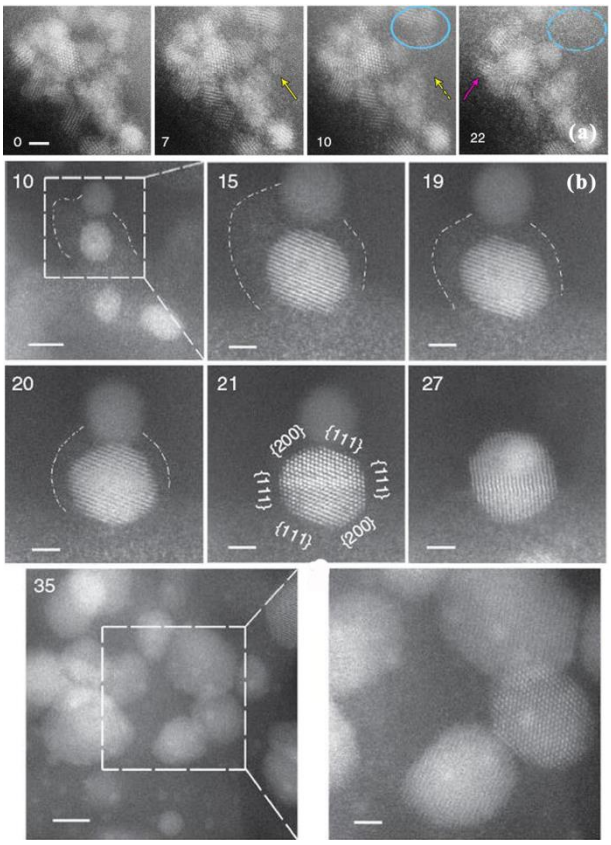

Figure 29 (a) Sequential images showing the dissociation of 2-3 nm particles and the formation of atom 'clouds' during in situ calcination at 500 °C in 150-torr O_2. The elapsed time (in minutes) is indicated on the lower left corner of each image. Arrows and ovals of the same color are used to indicate the gradual disappearance of the small crystallites. Scale bars are 2 nm. (b) Structural evolution following atom cloud formation. Sequential images taken at 650 °C in 150-torr O_2, showing the gradual disappearance of an atom 'clouds' accompanied by the growth of a particle in its close vicinity, followed by particle coalescence. The dashed line is used to delineate the periphery of the atom 'clouds'. The elapsed time (in minutes) is indicated on the upper left corner of each image. The scale bar is 5 nm (10), 2 nm (15-27), 5 nm (left panel) and 2 nm (right panel) for 35. Reproduced with permission.[74] Copyright 2015, Springer Nature.

5. 3D Electron Microscopy

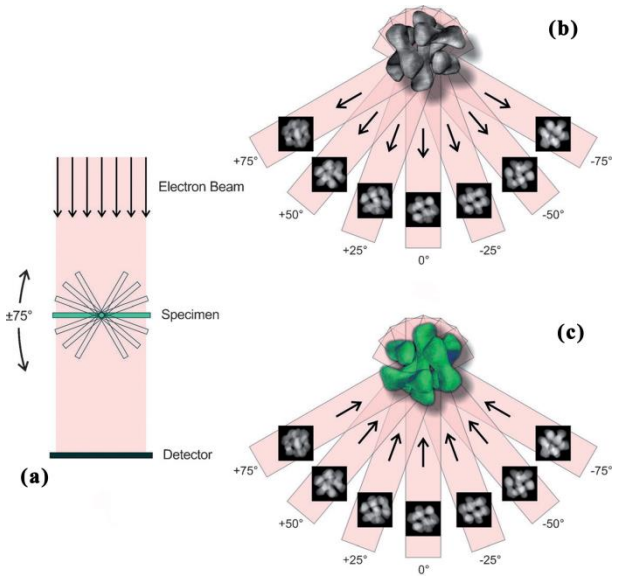

Figure 30 Illustration of a continuous electron tomography experiment, including the acquisition of a tilt series (a, b) and back-projection of the images along their original acquisition directions (c). Reproduced with permission.[6b] Copyright 2014, Wiley.

Although TEM is an ideal tool to provide information on the morphology, chemical composition and atomic structure of CeO_2-based nanocatalysts, it is still limited by the fact that the images only correspond to 2D projections of 3D nanostructures. Therefore, the outcome of a 2D analysis may be incomplete or even misleading.[14c, 75] This is particularly the case for CeO_2 nanostructures, where different reducibility and catalytic activity is expected for different surface facets such as {100}, {110} and {111}. Since the heterogeneous catalytic performance is mainly determined by the surface chemistry, a completely 3D characterization of both the structure and chemistry of the CeO_2-based nanostructures will undoubtedly provide new information.[76] 3D electron microscopy, or so-called "electron tomography", is a technique that yields a 3D reconstruction of a (nano)material based on a tilt series of its 2D projection HAADF-STEM images (Figure 30).[6b, 77] Nanometer scale resolution can be routinely obtained, but recently, 3D reconstructions with atomic resolution have also been obtained.[78] In addition

to a 3D structural characterization, analytical information (composition, oxidation state) can now also be obtained in 3D by expanding EDX and EELS from 2D to 3D.

5.1 HAADF-STEM electron tomography

As illustrated in Fig. 31, electron tomography is a very useful technique to study the surface and 3D morphology of synthesized CeO_2 nanoparticles.[79] Figure 31a, b shows

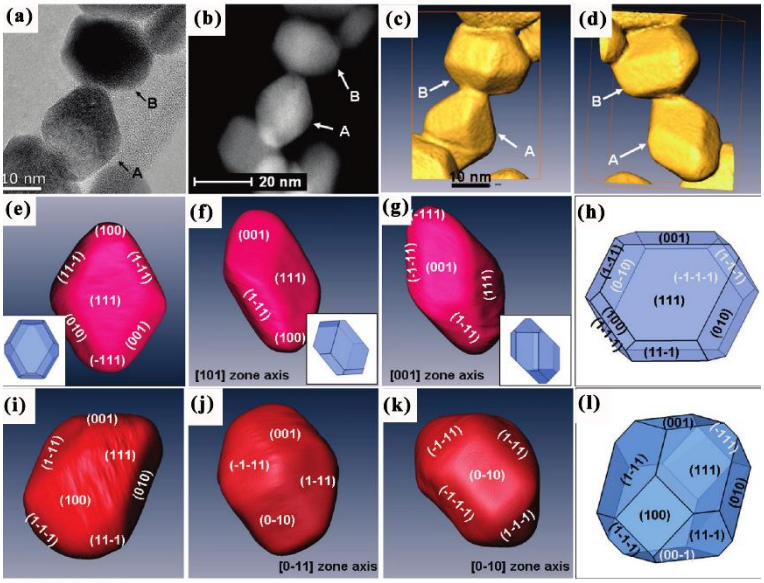

Figure 31 (a) Bright-field and (b) HAADF-STEM image of the same area containing large CeO_2 particles. (c) Top and (d) Iso-surface rendering view of the reconstructed 3D volume of the particles. (e) Surface rendering view of particle A after segmentation viewed along (f) [101] and (g) [001]. (i) Surface rendering view of particle B after segmentation and viewed along (j) [011] and (k) [010]. (h, l) Schematic drawing of the structure of particles A and B. Reproduced with permission.[79] Copyright 2011, American Chemical Society.

bright-field TEM and HAADF-STEM images of the same CeO_2 nanoparticles. Although the particles A and B appear to have a distinct morphology in the projected 2D images, the reconstructed 3D results clearly show that both particles have an irregular truncated octahedral shape, with eight {111} and six {100} facets. Viewing the reconstructed 3D models along

different orientations clearly highlights the real 3D shape of the irregular octahedral CeO_2 nanoparticles. Not only CeO_2 octahedra, but also cubes or nanorods have been characterized in this manner.[80] By using the geometrical parameters previously deduced, the relative amount of the different surfaces for the cubes can be determined as 86% {100}, 10% {110} and 4% {111}. For octahedra, the contribution of 2% {110} is quite insignificant compared to 98% {111}. A surprise is the direct evidence of a porous network inside the nanorods, with porous characteristics depending on the size of the rods (lamellar or cylindrical pores).[80] Similar results are also found for doped CeO_{2-x} (5wt% Fe) nanoparticles. An orthoslice through the reconstructed volume demonstrates the presence of voids inside the CeO_{2-x} (5wt% Fe) nanoparticles but not at the surface.[25] The presence of an inner substructure provides some extra corrugation of the surface which results in a higher exposed area, a property of high relevance for applications related to catalysis. In this way, electron tomography is able to solve the 3D and inner structure of nanoparticles that cannot be obtained using conventional 2D TEM.

5.2 STEM-EELS electron tomography

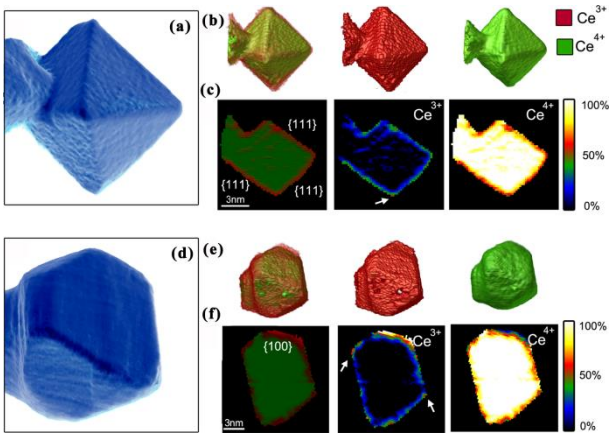

Figure 32 3D valence measurements. (a, d) HAADF-STEM reconstructions of a near-perfect and a truncated octahedral CeO_2 nanoparticle. (b, e) Corresponding 3D visualizations of the nanoparticles showing the valence results for Ce^{3+} and Ce^{4+}. (c, f) Slices through the Ce^{3+} and Ce^{4+} volumes, yielding a quantitative distribution of the reduced Ce ions. These slices indicate a thicker Ce^{3+} layer with the presence of more oxygen vacancies at the {001} truncation. Reproduced with permission.[14c] Copyright 2014, American Chemical Society.

Any successful implementation of CeO_2-based nanostructures in current and future applications strongly depends on a thorough understanding of their connection between the physical properties and the 3D structure and composition. HAADF-STEM electron tomography provides a general approach to study this relation. [14c, 80] However, it is important to note that the catalytic activity of CeO_2 is strongly related to its flexible reduction and oxidation behavior. This is connected to the possibility of switching between Ce^{4+} and Ce^{3+} oxidation states and the corresponding ability to release and take up oxygen at the surface of the nanoparticles through the formation of oxygen vacancies.[3c, 31a, 81] Recently, the valence change from Ce^{4+} and Ce^{3+} has been observed by STEM in combination with spatially resolved EELS, and the extent of the reduced shells has been investigated as a function of particle size.[14a] It should be stressed that unambiguous conclusions could impossibly be drawn from

2D projection data only. Thus, the exploration of valence state changes in 3D will undoubtedly provide a deeper understanding of the catalytic mechanism of CeO_2-based nanostructures.

Figure 32b, e shows 3D visualizations of the regions corresponding to Ce^{3+} (red) and Ce^{4+} (green) of CeO_2 with octahedral and truncated octahedral morphologies, respectively.[14c] By inspecting slices through the reconstruction, a uniform shell thickness for the {111} facets can be observed. For the octahedral CeO_2 particle, it seems there is an even Ce^{3+} signal on all facets. The tomographic nature of the technique also provides information on internal valency changes within the material. In this manner, the boundary between the two nanoparticles in Figure 32a is demonstrated to remain fully oxidized. For the truncated CeO_2 particle, the shell is observed to be thicker along a {001} surface plane compared with the {111} planes, as indicated in Figure 32f. The 3D approach has the additional benefit of delivering quantitative data for the cerium oxidation state. The quantitative data shown in Figure 32c evidences that at a {111} surface plane approximately 20-30 percent of the ceria ions are reduced. The reduction shell has an approximate thickness of 0.8±0.2 nm. It is fascinating to see that at corners the surface reduction can be elevated, up to a maximum value at the bottom corner of the octahedron of 54 percent Ce reduction (arrows). In the case of the truncated octahedron (Fig. 32f), the {001} surface facet shows a higher degree of surface reduction (±50 percent Ce ions in a reduced state) over a thicker measured shell (1.4±0.2 nm). Once again, the corners formed by the {111} surface facets show a tendency for a higher degree of Ce reduction (arrows).

Doped CeO_2 nanostructures have been developed extensively for a variety of catalytic reactions. Investigation of the spatial distribution and the valence state of dopants in CeO_2 nanostructures is therefore of great importance.[47a, 47c] As an example, Goris et al. measured the spatial distribution of Fe dopants in CeO_2 in 3D by so-called "direct spectroscopic electron tomography".[82] Figure 33a, b shows 3D renderings of both the HAADF-STEM reconstruction and the EELS reconstructions for Fe^{2+}, Fe^{3+}, Ce^{3+} and Ce^{4+}. As shown in Figure 33a, no

significant Fe^{3+} signal was detected. The thickness of the Ce^{3+} shell approximately equals 1.9 nm, which is consistent with previous studies (Figure 33b).[25] Moreover, it was found that most of the Fe dopants are located near the voids of the nanoparticles and the presence of the Fe^{2+} dopants (highlighted by the white arrows in Figure 33b) is correlated with a reduction of the Ce atoms from Ce^{4+} towards Ce^{3+}. This indicates that both Fe dopants and Ce are reduced by the generation of oxygen vacancies. This information cannot be extracted from a single 2D projection image in a straightforward manner because only a small amount of Ce^{3+} is projected simultaneously with a larger number of Ce^{4+}.

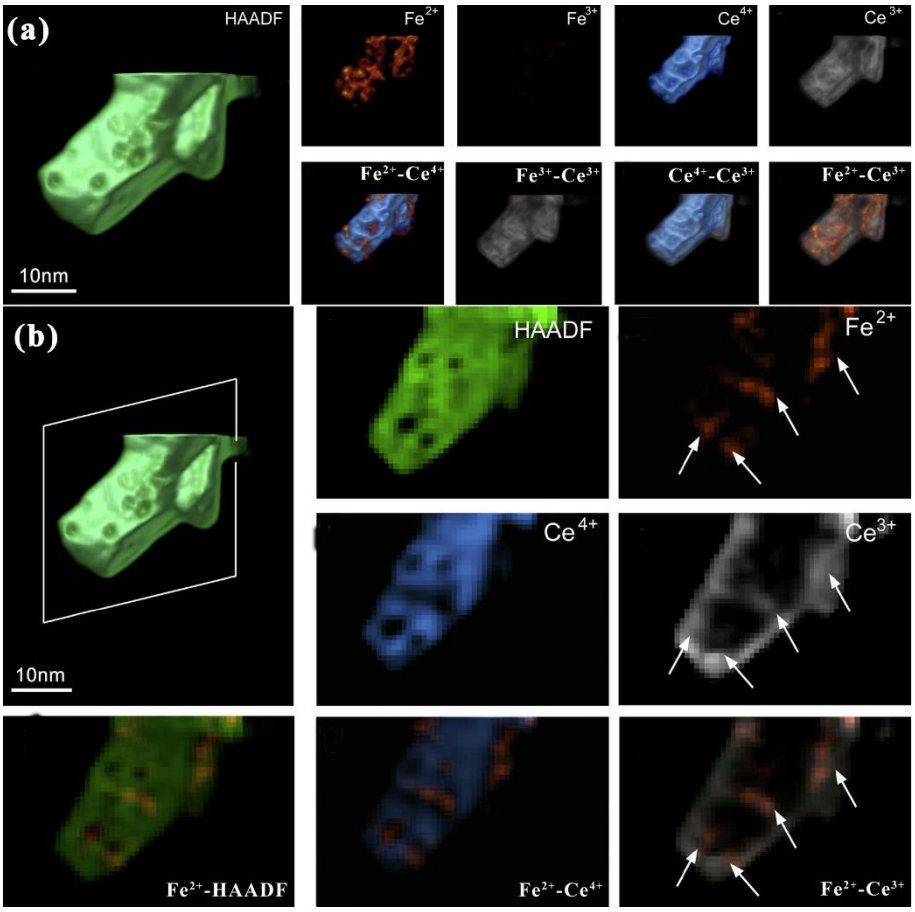

Figure 33 (a) HAADF-STEM reconstruction showing the morphology of Fe doped CeO_2, 3D visualizations of the reconstructed Fe^{2+}, Fe^{3+}, Ce^{3+} and Ce^{4+} signal, respectively. A negligible Fe^{3+} signal is present in the reconstruction which is in agreement with the 2D STEM-EELS results. (b) 3D visualization of the HAADF-STEM reconstruction with the representative slice

of Fe^{2+}, Ce^{4+}, and Ce^{3+}. As indicated by the white arrows, most Fe dopants are present near the voids of the nanoparticle and the presence of Fe^{2+} dopants is often correlated with a reduction of the Ce nanoparticle from Ce^{4+} to Ce^{3+}. Reproduced with permission.[82] Copyright 2016, Elsevier.

By using a new model-based EELS electron tomography approach, Collins et al. revealed the surface segregation of dopant cations, oxygen vacancies as well as bonding changes in lanthanum-doped CeO_2 (LDC) nanoparticle aggregates with sub-nanometer precision.[83] Signatures of Ce^{4+} were observed in the core, and signatures of Ce^{3+} in the shell (Figure 34b) whereas the La signal was observed both in the core and in the shell. The EELS fine structure analysis was extended to examine also the O *K* ionization edge, as shown in Figure 33c. Peak A disappeared in the shell spectrum, suggesting a loss of Ce(*4f*)-O(*2p*) orbital hybridization in the Ce^{3+} surface layer. Additionally, the shell spectrum (Figure 33c) is consistent with the appearance of additional electronic states at energies between the B and C peaks in Ce^{3+} oxides. Analysis of the La concentration suggested an enrichment of La at the surface. These measurements indicate surface segregation of La in LDC associated with the observed changes of the Ce valence state and Ce-O orbital hybridization. This result refines the understanding of the spatially varying electronic structure and bonding in CeO_2-based nanostructures with aliovalent cation concentrations.

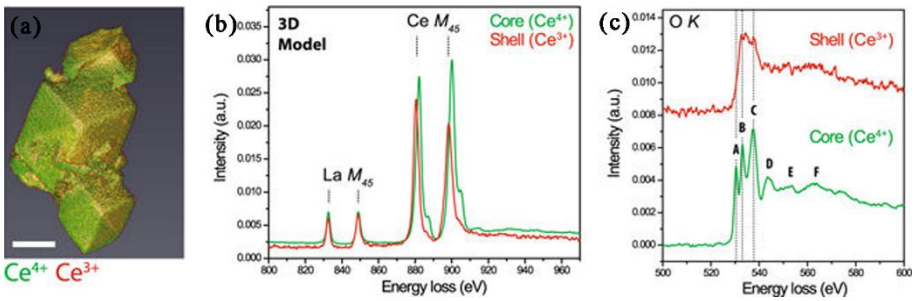

Figure 34 (a) 3D volume visualization of the core-shell aggregate. (b) Corresponding spectra at the La and Ce $M_{4,5}$ edges, and (c) corresponding spectra at the O *K* edge (Ce and O edges

are both from the second aggregate). Dashed lines and letters indicate spectral features attributed to characteristic orbital hybridization signatures. The three prominent peaks were assigned as (A) Ce(*4f*)-O(*2p*), (B) Ce(*5d* e_g)-O(*2p*), and (C) Ce(*5d* t_{2g})-O(*2p*). Scale bars are 25 nm. Reproduced with permission.[83] Copyright 2017, Springer.

6. Conclusions and Outlook

Advanced (scanning) transmission electron microscopy has contributed significantly to the research of CeO_2-based nanostructures. The exact atomic arrangement of different surfaces and grain boundaries of CeO_2 can be revealed by *AC*-TEM. The results are valuable for theoretical calculations to establish reliable models towards the design of novel catalysts at the atomic level. The dynamic reconstruction of the surface has been systematically explored, clarifying the surface chemistry compared with bulk materials. Combined with EELS, the surface reduction (from Ce^{4+} to Ce^{3+}) of different facets has been studied down to atomic scale, suggesting more reducibility on {100} surfaces. This helps to explain the superior catalytic efficiency on these {100} surfaces. HAADF-STEM electron tomography reveals the 3D morphology influence on the catalytic performance. The valence state changes and distribution of Ce^{3+}/Ce^{4+} in 3D can be demonstrated by STEM-EELS electron tomography, providing a deep understanding on the catalytic mechanism of CeO_2-based nanostructures. Detailed information on the sintering mechanism is also obtained from in-situ TEM experiments. The metal-support interfaces in several M-CeO_2 heterogeneous catalysts have been investigated by combining atomic resolution STEM imaging and EELS analysis both in static and environmental conditions, providing direct proof of the interfacial atomic structure and oxidation states. These progresses are impressive but more systematic work is still needed; the contribution of advanced electron microscopy and novel developments in the field of (in situ) sample holders and detectors can be substantial.

The growth mechanism of CeO_2-based nanostructures is still controversial, which limits the needed insight to design novel CeO_2-based nanocatalysts. The main problem is that most TEM/STEM studies are fragmented. Liquid cell TEM provides an opportunity to monitor nanocrystal growth in situ, which can assist in elucidating the growth mechanisms of different nanocrystals.[84] Especially, since atomic scale resolution has been obtained using a graphene

liquid cell TEM, one can envisage to discover unexplored mechanisms of colloidal nanocrystal growth.[85] Experiments on liquid-phase growth of CeO_2 are certainly to be performed in the near future; this will allow to obtain direct evidence on the morphology controllable synthesis of CeO_2.

Electron tomography enables the analysis of the 3D morphology effect of CeO_2, however, the whole process is time-consuming and can eventually lead to beam damage on the sample during the tilt series. Further work is still needed to reduce the recording time of electron tomography, while still providing trustworthy, quantitative results. 3D atomic resolution in most CeO_2-based nanostructures is still elusive, indicating that new and more flexible algorithmic approaches are needed to improve both the reconstruction fidelity and resolution.

The recent advancements in *AC*-TEM make it possible to obtain atomic resolution information on the metal-support interfaces in several M-CeO_2 nanocatalysts. However, many fundamental questions relative to interfaces remain unanswered, particularly regarding the dynamic processes, charge distribution and transfer processes in supported metal nanocatalysts. Morphology changes of the supported nanoparticles happen on a time scale of seconds or minutes, but, the study of the electronic state changes in the interface may require picosecond time resolution.[4h, 75b] Therefore, ultrafast TEM is needed to provide a true understanding of the dynamic reactions at the interface.

Despite the enormous progress made in the field of in-situ TEM, there is still a long way to go with respect to atomic level characterization of chemistry (composition, oxide state, and electron structure) of surfaces and interfaces under catalytic conditions. One limitation is the upper pressure in many in-situ studies. Another problem is the reduced resolution due to thermal drift at relatively high temperatures.[64-65] Recent applications of microelectromechanical systems (MEMS) technology permit a much higher pressure to be

maintained and minimizes the thermal drift.[4h, 86] In situ (E)TEM studies at atomic resolution, using MEMS-based windowed cells, will have to be conducted to explore nanocatalysts at elevated temperatures and high pressure. This could dramatically accelerate our understanding of the composition-structure-property relations in CeO_2-based nanostructures.

Acknowledgement

Yang Zhang acknowledges financial support from the European Union's Horizon 2020 research and innovation programme under the Marie Skłodowska-Curie grant agreement No 665501 through a FWO [PEGASUS]^2 Marie Skłodowska-Curie fellowship (12U4917N), SB acknowledge funding from the European Research Council, ERC grant No. 335078-Colouratom.

Received: ((will be filled in by the editorial staff))

Revised: ((will be filled in by the editorial staff))

Published online: ((will be filled in by the editorial staff))

REFERENCE:

[1] a) K. Wu, L.-D. Sun, C.-H. Yan, *Adv. Energy Mater.* **2016**, 6, 1600501; b) H. Dong, S.-R. Du, X.-Y. Zheng, G.-M. Lyu, L.-D. Sun, L.-D. Li, P.-Z. Zhang, C. Zhang, C.-H. Yan, *Chem. Rev.* **2015**, 115, 10725; c) T. Montini, M. Melchionna, M. Monai, P. Fornasiero, *Chem. Rev.* **2016**, 116, 5987; d) J. A. Rodriguez, D. C. Grinter, Z. Liu, R. M. Palomino, S. D. Senanayake, *Chem. Soc. Rev.* **2017**, 46, 1824; e) S. D. Senanayake, D. Stacchiola, J. A. Rodriguez, *Acc. Chem. Res.* **2013**, 46, 1702; f) A. Trovarelli, J. Llorca, *ACS Catal.* **2017**, 7, 4716; g) S. Xie, Z. Wang, F. Cheng, P. Zhang, W. Mai, Y. Tong, *Nano Energy* **2017**, 34, 313.

[2] a) C. Sun, H. Li, L. Chen, *Energy Environ. Sci.* **2012**, 5, 8475; b) Y. Li, W. Shen, *Chem. Soc. Rev.* **2014**, 43, 1543; c) T. Yu, J. Joo, Y. I. Park, T. Hyeon, *Angew. Chem. Int. Ed.* **2005**, 117, 7577; d) S. Yang, L. Gao, *J. Am. Chem. Soc.* **2006**, 128, 9330; e) U. M. Bhatta, D. Reid, T. Sakthivel, T. X. Sayle, D. Sayle, M. Molinari, S. C. Parker, I. M. Ross, S. Seal, G. n. Möbus, *J. Phys. Chem. C* **2013**, 117, 24561.

[3] a) Tana, M. Zhang, J. Li, H. Li, Y. Li, W. Shen, *Catalysis Today* **2009**, 148, 179; b) E. Aneggi, D. Wiater, C. de Leitenburg, J. Llorca, A. Trovarelli, *ACS Catal.* **2014**, 4, 172; c) J.-D. Cafun, K. O. Kvashnina, E. Casals, V. F. Puntes, P. Glatzel, *ACS Nano* **2013**, 7, 10726; d) J. Lv, Y. Shen, L. Peng, X. Guo, W. Ding, *Chem. Commun.* **2010**, 46, 5909; e) K. Reed, A. Cormack, A. Kulkarni, M. Mayton, D. Sayle, F. Klaessig, B. Stadler, *Environ. Sci.: Nano* **2014**, 1, 390; f) Y. Ding, Y. Chen, K. C. Pradel, M. Liu, Z. L. Wang, *J. Appl. Phys.* **2016**, 120, 214302; g) R. C. Merrifield, K. P. Arkill, R. E. Palmer, J. R. Lead, *Environ. Sci. Technol.* **2017**, 51, 8010; h) L. Sun, D. Marrocchelli, B. Yildiz, *Nat. Commun.* **2015**, 6, 6294.

[4] a) J. Wu, H. Shan, W. Chen, X. Gu, P. Tao, C. Song, W. Shang, T. Deng, *Adv. Mater.* **2016**, 28, 9686; b) G. Van Tendeloo, S. Bals, S. Van Aert, J. Verbeeck, D. Van Dyck,

Adv. Mater. **2012**, 24, 5655; c) P. D. Nellist, M. F. Chisholm, N. Dellby, O. Krivanek, M. Murfitt, Z. Szilagyi, A. R. Lupini, A. Borisevich, W. Sides, S. J. Pennycook, *Science* **2004**, 305, 1741; d) M. P. Oxley, A. R. Lupini, S. J. Pennycook, *Rep. Prog. Phys.* **2016**, 80, 026101; e) L. H. Tizei, R. Nakanishi, R. Kitaura, H. Shinohara, K. Suenaga, *Phys. Rev. Lett.* **2015**, 114, 197602; f) W. Zhang, W. Zheng, *Adv. Funct. Mater.* **2016**, 26, 2988; g) S. Ida, S. Koga, T. Daio, H. Hagiwara, T. Ishihara, *Angew. Chem. Int. Ed.* **2014**, 53, 13078; h) F. Tao, P. A. Crozier, *Chem. Rev.* **2016**, 116, 3487; i) S. I. Sanchez, M. W. Small, S. Sivaramakrishnan, J.-g. Wen, J.-M. Zuo, R. G. Nuzzo, *Anal. Chem.* **2010**, 82, 2599; j) X. Y. Shi, W. Zhang, C. Zhang, W. T. Zheng, H. Chen, J. G. Qi, *J. Microscopy* **2016**, 262, 203; k) P. Koirala, Y. Lin, J. Ciston, L. D. Marks, *Ultramicroscopy* **2016**, 170, 35.

[5] a) D. S. Su, B. Zhang, R. Schlögl, *Chem. Rev.* **2015**, 115, 2818; b) W. Gao, Z. D. Hood, M. Chi, *Acc. Chem. Res.* **2017**, 50, 787; c) R. Yu, L. H. Hu, Z. Y. Cheng, Y. D. Li, H. Q. Ye, J. Zhu, *Phys. Rev. Lett.* **2010**, 105, 226101; d) R. Ishikawa, R. Mishra, A. R. Lupini, S. D. Findlay, T. Taniguchi, S. T. Pantelides, S. J. Pennycook, *Phys. Rev. Lett.* **2014**, 113, 155501; e) H. Tan, S. Turner, E. Yücelen, J. Verbeeck, G. Van Tendeloo, *Phys. Rev. Lett.* **2011**, 107, 107602.

[6] a) R. Leary, P. A. Midgley, J. M. Thomas, *Acc. Chem. Res.* **2012**, 45, 1782; b) S. Bals, B. Goris, L. M. Liz-Marzán, G. Van Tendeloo, *Angew. Chem. Int. Ed.* **2014**, 53, 10600; c) Z. Saghi, P. A. Midgley, *Ann. Rev. Mater. Res.* **2012**, 42, 59; d) D. Van Dyck, F.-R. Chen, *Nature* **2012**, 486, 243.

[7] a) A. Genc, L. Kovarik, M. Gu, H. Cheng, P. Plachinda, L. Pullan, B. Freitag, C. Wang, *Ultramicroscopy* **2013**, 131, 24; b) S. M. Collins, P. A. Midgley, *Ultramicroscopy* **2017**, 180, 133; c) P. Torruella, R. Arenal, F. de la Peña, Z. Saghi, L. Yedra, A. Eljarrat, L. López-Conesa, M. Estrader, A. López-Ortega, G. Salazar-Alvarez, J. Nogués, C. Ducati,

P. A. Midgley, F. Peiró, S. Estradé, *Nano Lett.* **2016**, 16, 5068; d) K. J. Batenburg, S. Bals, J. Sijbers, C. Kübel, P. A. Midgley, J. C. Hernandez, U. Kaiser, E. R. Encina, E. A. Coronado, G. Van Tendeloo, *Ultramicroscopy* **2009**, 109, 730; e) O. Ersen, I. Florea, C. Hirlimann, C. Pham-Huu, *Mater. Today* **2015**, 18, 395.

[8] a) Y. Jiang, H. Li, Z. Wu, W. Ye, H. Zhang, Y. Wang, C. Sun, Z. Zhang, *Angew. Chem. Int. Ed.* **2016**, 128, 12615; b) H. L. Xin, S. Alayoglu, R. Tao, A. Genc, C.-M. Wang, L. Kovarik, E. A. Stach, L.-W. Wang, M. Salmeron, G. A. Somorjai, H. Zheng, *Nano Lett.* **2014**, 14, 3203; c) C. Luo, C. Wang, X. Wu, J. Zhang, J. Chu, *Small* **2017**, 13, 1604259; d) K.-Y. Niu, J. Park, H. Zheng, A. P. Alivisatos, *Nano Lett.* **2013**, 13, 5715; e) M. Hauser, M. Wojcik, D. Kim, M. Mahmoudi, W. Li, K. Xu, *Chem. Rev.* **2017**, 117, 7428; f) D. A. Muller, *Nat Mater* **2009**, 8, 263.

[9] Z. L. Wang, X. Feng, *J. Phys. Chem. B* **2003**, 107, 13563.

[10] E. Shoko, M. Smith, R. H. McKenzie, *J. Phys. Condens. Mat.* **2010**, 22, 223201.

[11] Y. Li, X. He, J.-J. Yin, Y. Ma, P. Zhang, J. Li, Y. Ding, J. Zhang, Y. Zhao, Z. Chai, Z. Zhang, *Angew. Chem. Int. Ed.* **2015**, 54, 1832.

[12] a) M. Nolan, S. C. Parker, G. W. Watson, *Surf. Sci.* **2005**, 595, 223; b) M. Nolan, S. Grigoleit, D. C. Sayle, S. C. Parker, G. W. Watson, *Surf. Sci.* **2005**, 576, 217.

[13] a) J. Paier, C. Penschke, J. Sauer, *Chem. Rev.* **2013**, 113, 3949; b) D. R. Mullins, P. M. Albrecht, F. Calaza, *Top. Catal.* **2013**, 56, 1345.

[14] a) S. Turner, S. Lazar, B. Freitag, R. Egoavil, J. Verbeeck, S. Put, Y. Strauven, G. Van Tendeloo, *Nanoscale* **2011**, 3, 3385; b) M. Panahi-Kalamuei, S. Alizadeh, M. Mousavi-Kamazani, M. Salavati-Niasari, *J. Ind. Eng. Chem.* **2015**, 21, 1301; c) B. Goris, S. Turner, S. Bals, G. Van Tendeloo, *ACS Nano* **2014**, 8, 10878.

[15] a) M. A. Cordeiro, W. Weng, D. G. Stroppa, C. J. Kiely, E. R. Leite, *Chem. Mater.* **2013**, 25, 2028; b) Y. Yang, Y. Jin, H. He, Z. Ye, *CrystEngComm* **2010**, 12, 2663; c)

L. González-Rovira, J. M. Sánchez-Amaya, M. López-Haro, E. del Rio, A. B. Hungría, P. Midgley, J. J. Calvino, S. Bernal, F. J. Botana, *Nano Lett.* **2009**, 9, 1395; d) A. C. Johnston-Peck, J. P. Winterstein, A. D. Roberts, J. S. DuChene, K. Qian, B. C. Sweeny, Wei D. Wei, R. Sharma, E. A. Stach, A. A. Herzing, *Ultramicroscopy* **2016**, 162, 52.

[16] Y. Lin, Z. Wu, J. Wen, K. R. Poeppelmeier, L. D. Marks, *Nano Lett.* **2013**, 14, 191.

[17] a) S. Agarwal, L. Lefferts, B. L. Mojet, D. Ligthart, E. J. Hensen, D. R. Mitchell, W. J. Erasmus, B. G. Anderson, E. J. Olivier, J. H. Neethling, *ChemSusChem* **2013**, 6, 1898; b) T. X. T. Sayle, M. Cantoni, U. M. Bhatta, S. C. Parker, S. R. Hall, G. Möbus, M. Molinari, D. Reid, S. Seal, D. C. Sayle, *Chem. Mater.* **2012**, 24, 1811; c) C. Yang, X. Yu, S. Heißler, A. Nefedov, S. Colussi, J. Llorca, A. Trovarelli, Y. Wang, C. Wöll, *Angew. Chem. Int. Ed.* **2017**, 56, 375.

[18] a) Y. Lin, J. Wen, L. Hu, R. M. Kennedy, P. C. Stair, K. R. Poeppelmeier, L. D. Marks, *Phys. Rev. Lett.* **2013**, 111, 156101; b) W. Zhang, W. T. Zheng, *Phys. Chem. Chem. Phys.* **2015**, 17, 14461.

[19] S. J. Haigh, N. P. Young, H. Sawada, K. Takayanagi, A. I. Kirkland, *ChemPhysChem* **2011**, 12, 2397.

[20] J. Huang, Y. Yu, J. Zhu, R. Yu, *Sci. China Mater.* **2017**, 60, 903.

[21] a) G. Möbus, Z. Saghi, D. C. Sayle, U. M. Bhatta, A. Stringfellow, T. X. T. Sayle, *Adv. Funct. Mater.* **2011**, 21, 1971; b) U. M. Bhatta, I. M. Ross, T. X. T. Sayle, D. C. Sayle, S. C. Parker, D. Reid, S. Seal, A. Kumar, G. Möbus, *ACS Nano* **2012**, 6, 421.

[22] a) D. C. Sayle, S. A. Maicaneanu, G. W. Watson, *J. Am. Chem. Soc.* **2002**, 124, 11429; b) W. Gao, Z. Zhang, J. Li, Y. Ma, Y. Qu, *Nanoscale* **2015**, 7, 11686.

[23] T. Sayle, S. Parker, C. Catlow, *Surf. Sci.* **1994**, 316, 329.

[24] a) F. Zhang, P. Wang, J. Koberstein, S. Khalid, S.-W. Chan, *Surf. Sci.* **2004**, 563, 74; b) S. Torbrügge, M. Reichling, A. Ishiyama, S. Morita, O. Custance, *Phys. Rev. Lett.* **2007**, 99, 056101.

[25] M. Meledina, S. Turner, V. Galvita, H. Poelman, G. Marin, G. Van Tendeloo, *Nanoscale* **2015**, 7, 3196.

[26] a) J. Verbeeck, S. Van Aert, *Ultramicroscopy* **2004**, 101, 207; b) J. Verbeeck, S. Van Aert, G. Bertoni, *Ultramicroscopy* **2006**, 106, 976; c) J. Verbeeck, G. Bertoni, *Ultramicroscopy* **2008**, 108, 74; d) G. Bertoni, J. Verbeeck, *Ultramicroscopy* **2008**, 108, 782.

[27] a) W. Lee, H. J. Jung, M. H. Lee, Y. B. Kim, J. S. Park, R. Sinclair, F. B. Prinz, *Adv. Funct. Mater.* **2012**, 22, 965; b) X. Guo, R. Waser, *Prog. Mater. Sci.* **2006**, 51, 151; c) Y.-M. Kim, J. He, M. D. Biegalski, H. Ambaye, V. Lauter, H. M. Christen, S. T. Pantelides, S. J. Pennycook, S. V. Kalinin, A. Y. Borisevich, *Nat. Mater.* **2012**, 11, 888.

[28] H. Hojo, T. Mizoguchi, H. Ohta, S. D. Findlay, N. Shibata, T. Yamamoto, Y. Ikuhara, *Nano Lett.* **2010**, 10, 4668.

[29] S. D. Findlay, N. Shibata, H. Sawada, E. Okunishi, Y. Kondo, Y. Ikuhara, *Ultramicroscopy* **2010**, 110, 903.

[30] B. Feng, I. Sugiyama, H. Hojo, H. Ohta, N. Shibata, Y. Ikuhara, *Sci. Rep.* **2016**, 6.

[31] a) Z.-A. Qiao, Z. Wu, S. Dai, *ChemSusChem* **2013**, 6, 1821; b) T. X. Sayle, S. C. Parker, D. C. Sayle, *Chem. Commun.* **2004**, 2438; c) M. Lu, Y. Zhang, Y. Wang, M. Jiang, X. Yao, *ACS Appl. Mater. Interfaces* **2016**, 8, 23580; d) J. Zhang, H. Kumagai, K. Yamamura, S. Ohara, S. Takami, A. Morikawa, H. Shinjoh, K. Kaneko, T. Adschiri, A. Suda, *Nano Lett.* **2011**, 11, 361; e) K. Zhou, Y. Li, *Angew. Chem. Inter. Ed.* **2012**, 51, 602; f) E. W. Zhao, H. Zheng, R. Zhou, H. E. Hagelin-Weaver, C. R. Bowers, *Angew. Chem. Inter. Ed.* **2015**, 54, 14270; g) H. Tan, J. Wang, S. Yu, K. Zhou, *Environ. Sci.*

Technol. **2015**, 49, 8675; h) T. X. Sayle, F. Caddeo, X. Zhang, T. Sakthivel, S. Das, S. Seal, S. Ptasinska, D. C. Sayle, *Chem. Mater.* **2016**, 28, 7287.

[32] K. Zhou, X. Wang, X. Sun, Q. Peng, Y. Li, *J. Catal.* **2005**, 229, 206.

[33] Z. Wu, M. Li, S. H. Overbury, *J. Catal.* **2012**, 285, 61.

[34] H.-X. Mai, L.-D. Sun, Y.-W. Zhang, R. Si, W. Feng, H.-P. Zhang, H.-C. Liu, C.-H. Yan, *J. Phys. Chem. B* **2005**, 109, 24380.

[35] a) L. Wu, H. Wiesmann, A. Moodenbaugh, R. Klie, Y. Zhu, D. Welch, M. Suenaga, *Phys. Rev. B* **2004**, 69, 125415; b) M. C. Spadaro, P. Luches, G. Bertoni, V. Grillo, S. Turner, G. Van Tendeloo, S. Valeri, S. D'Addato, *Nanotechnology* **2016**, 27, 425705.

[36] R. K. Hailstone, A. G. DiFrancesco, J. G. Leong, T. D. Allston, K. J. Reed, *J. Phys. Chem. C* **2009**, 113, 15155.

[37] W.-Q. Han, L. Wu, Y. Zhu, *J. Am. Chem. Soc.* **2005**, 127, 12814.

[38] S. Deshpande, S. Patil, S. V. Kuchibhatla, S. Seal, *Appl. Phys. Lett.* **2005**, 87, 133113.

[39] M. Lin, Z. Y. Fu, H. R. Tan, J. P. Y. Tan, S. C. Ng, E. Teo, *Cryst. Growth Des.* **2012**, 12, 3296.

[40] a) J. Zhang, S. Ohara, M. Umetsu, T. Naka, Y. Hatakeyama, T. Adschiri, *Adv. Mater.* **2007**, 19, 203; b) X. Wang, J. Zhuang, Q. Peng, Y. Li, *Nature* **2005**, 437, 121; c) M. Rycenga, C. M. Cobley, J. Zeng, W. Li, C. H. Moran, Q. Zhang, D. Qin, Y. Xia, *Chem. Rev.* **2011**, 111, 3669.

[41] X. Liang, J. Xiao, B. Chen, Y. Li, *Inorg. Chem.* **2010**, 49, 8188.

[42] a) F. Dang, K. Kato, H. Imai, S. Wada, H. Haneda, M. Kuwabara, *Cryst. Growth Des.* **2010**, 10, 4537; b) R. L. Penn, J. F. Banfield, *Science* **1998**, 281, 969.

[43] N. Du, H. Zhang, B. Chen, X. Ma, D. Yang, *J. Phys. Chem. C* **2007**, 111, 12677.

[44] P. Huang, F. Wu, B. Zhu, X. Gao, H. Zhu, T. Yan, W. Huang, S. Wu, D. Song, *J. Phys. Chem. B* **2005**, 109, 19169.

[45] Z. Ji, X. Wang, H. Zhang, S. Lin, H. Meng, B. Sun, S. George, T. Xia, A. E. Nel, J. I. Zink, *ACS Nano* **2012**, 6, 5366.

[46] a) X. Liang, X. Wang, Y. Zhuang, B. Xu, S. Kuang, Y. Li, *J. Am. Chem. Soc.* **2008**, 130, 2736; b) R. Wang, P. A. Crozier, R. Sharma, J. B. Adams, *Nano Lett.* **2008**, 8, 962; c) A. Pappacena, M. Rancan, L. Armelao, J. Llorca, W. Ge, B. Ye, A. Lucotti, A. Trovarelli, M. Boaro, *J. Phy. Chem. C* **2017**, 121, 17746.

[47] a) J. S. Elias, M. Risch, L. Giordano, A. N. Mansour, Y. Shao-Horn, *J. Am. Chem. Soc.* **2014**, 136, 17193; b) J. S. Elias, N. Artrith, M. Bugnet, L. Giordano, G. A. Botton, A. M. Kolpak, Y. Shao-Horn, *ACS Catal.* **2016**, 6, 1675; c) J. Ke, J.-W. Xiao, W. Zhu, H. Liu, R. Si, Y.-W. Zhang, C.-H. Yan, *J. Am. Chem. Soc.* **2013**, 135, 15191; d) H. Y. Kim, M. S. Hybertsen, P. Liu, *Nano Lett.* **2017**, 17, 348.

[48] a) T. Akita, M. Kohyama, M. Haruta, *Acc. Chem. Res.* **2013**, 46, 1773; b) F. Pilger, A. Testino, A. Carino, C. Proff, A. Kambolis, A. Cervellino, C. Ludwig, *ACS Cataly.* **2016**, 6, 3688; c) S. Colussi, A. Gayen, M. Farnesi Camellone, M. Boaro, J. Llorca, S. Fabris, A. Trovarelli, *Angew. Chem. Int. Ed.* **2009**, 48, 8481; d) F. Wang, S. He, H. Chen, B. Wang, L. Zheng, M. Wei, D. G. Evans, X. Duan, *J. Am. Chem. Soc.* **2016**, 138, 6298; e) L. Liu, Z. Yao, Y. Deng, F. Gao, B. Liu, L. Dong, *ChemCatChem* **2011**, 3, 978.

[49] A. Chen, Y. Zhou, N. Ta, Y. Li, W. Shen, *Cataly. Sci. Technol.* **2015**, 5, 4184.

[50] a) A. C. Johnston-Peck, S. D. Senanayake, J. J. Plata, S. Kundu, W. Xu, L. Barrio, J. s. Graciani, J. F. Sanz, R. M. Navarro, J. L. Fierro, *J. Phys. Chem. C* **2013**, 117, 14463; b) M. Tinoco, J. J. Sanchez, M. P. Yeste, M. Lopez-Haro, S. Trasobares, A. B. Hungria, P. Bayle-Guillemaud, G. Blanco, J. M. Pintado, J. J. Calvino, *ChemCatChem* **2015**, 7, 3763.

[51] S. Kundu, J. Ciston, S. D. Senanayake, D. A. Arena, E. Fujita, D. Stacchiola, L. Barrio, R. M. Navarro, J. L. Fierro, J. A. Rodriguez, *J. Phys. Chem. C* **2012**, 116, 14062.

[52] a) Q. Fu, T. Wagner, *Surf. Sci. Rep.* **2007**, 62, 431; b) H. Hattori, *Chem. Rev.* **1995**, 95, 537.

[53] T. Akita, S. Tanaka, K. Tanaka, M. Kohyama, *Mater. Sci. Forum* **2010**, 654-656, 2362.

[54] J.-L. Lu, H.-J. Gao, S. Shaikhutdinov, H.-J. Freund, *Cataly. Lett.* **2007**, 114, 8.

[55] a) T. Akita, K. Tanaka, M. Kohyama, M. Haruta, *Catal. Today* **2007**, 122, 233; b) T. Akita, M. Okumura, K. Tanaka, M. Kohyama, M. Haruta, *Catal. Today* **2006**, 117, 62; c) T. Akita, S. Tanaka, K. Tanaka, M. Haruta, M. Kohyama, *J. Mater. Sci.* **2011**, 46, 4384; d) T. Akita, K. Tanaka, M. Kohyama, *J. Mater. Sci.* **2008**, 43, 3917; e) Y.-G. Wang, D. Mei, V.-A. Glezakou, J. Li, R. Rousseau, *Nat. Commun.* **2015**, 6.

[56] F. Esch, S. Fabris, L. Zhou, T. Montini, C. Africh, P. Fornasiero, G. Comelli, R. Rosei, *Science* **2005**, 309, 752.

[57] Y. Lin, Z. Wu, J. Wen, K. Ding, X. Yang, K. R. Poeppelmeier, L. D. Marks, *Nano Lett.* **2015**, 15, 5375.

[58] T. Wu, X. Pan, Y. Zhang, Z. Miao, B. Zhang, J. Li, X. Yang, *J. Phys. Chem. Lett.* **2014**, 5, 2479.

[59] a) X. Wang, D. Liu, S. Song, H. Zhang, *J. Am. Chem. Soc.* **2013**, 135, 15864; b) Y. Gao, W. Wang, S. Chang, W. Huang, *ChemCatChem* **2013**, 5, 3610; c) L. Artiglia, F. Orlando, K. Roy, R. Kopelent, O. Safonova, M. Nachtegaal, T. Huthwelker, J. A. van Bokhoven, *J. Phys. Chem. Lett.* **2016**, 8, 102; d) S. B. Simonsen, I. Chorkendorff, S. Dahl, M. Skoglundh, J. Sehested, S. Helveg, *J. Am. Chem. Soc.* **2010**, 132, 7968.

[60] J. Jones, H. Xiong, A. T. DeLaRiva, E. J. Peterson, H. Pham, S. R. Challa, G. Qi, S. Oh, M. H. Wiebenga, X. I. P. Hernández, *Science* **2016**, 353, 150.

[61] a) R. Ouyang, J.-X. Liu, W.-X. Li, *J. Am. Chem. Soc.* **2013**, 135, 1760; b) J. Liu, *ACS Catal.* **2017**, 7, 34; c) L. Lin, W. Zhou, R. Gao, S. Yao, X. Zhang, W. Xu, S. Zheng, Z.

Jiang, Q. Yu, Y.-W. Li, *Nature* **2017**, 544, 80; d) B. Qiao, A. Wang, X. Yang, L. F. Allard, Z. Jiang, Y. Cui, J. Liu, J. Li, T. Zhang, *Nat. Chem.* **2011**, 3, 634.

[62] P. Luches, L. Giordano, V. Grillo, G. C. Gazzadi, S. Prada, M. Campanini, G. Bertoni, C. Magen, F. Pagliuca, G. Pacchioni, S. Valeri, *Adv. Mater. Interfaces* **2015**, 2, 1500375.

[63] a) S. Li, Y. Xu, Y. Chen, W. Li, L. Lin, M. Li, Y. Deng, X. Wang, B. Ge, C. Yang, S. Yao, J. Xie, Y. Li, X. Liu, D. Ma, *Angew. Chem. Int. Ed.* **2017**, 129, 10901; b) M. Cargnello, V. V. T. Doan-Nguyen, T. R. Gordon, R. E. Diaz, E. A. Stach, R. J. Gorte, P. Fornasiero, C. B. Murray, *Science* **2013**, 341, 771.

[64] M. A. L. Cordeiro, P. A. Crozier, E. R. Leite, *Nano Lett.* **2012**, 12, 5708.

[65] a) S. Zhang, L. Nguyen, Y. Zhu, S. Zhan, C.-K. Tsung, F. Tao, *Acc. Chem. Res.* **2013**, 46, 1731; b) Y. Li, L. Zang, D. L. Jacobs, J. Zhao, X. Yue, C. Wang, *Nat. Commun.* **2017**, 8.

[66] a) S. Liu, J. Xie, Q. Su, G. Du, S. Zhang, G. Cao, T. Zhu, X. Zhao, *Nano Energy* **2014**, 8, 84; b) R. A. Bernal, R. Ramachandramoorthy, H. D. Espinosa, *Ultramicroscopy* **2015**, 156, 23; c) Q. Li, P. Wang, Q. Feng, M. Mao, J. Liu, S. X. Mao, H. Wang, *Chem. Mater.* **2014**, 26, 4102.

[67] P. Gao, Z. Kang, W. Fu, W. Wang, X. Bai, E. Wang, *J. Am. Chem. Soc.* **2010**, 132, 4197.

[68] R. Wang, P. A. Crozier, R. Sharma, *J. Phys. Chem. C* **2009**, 113, 5700.

[69] P. A. Crozier, R. Wang, R. Sharma, *Ultramicroscopy* **2008**, 108, 1432.

[70] T. Uchiyama, H. Yoshida, Y. Kuwauchi, S. Ichikawa, S. Shimada, M. Haruta, S. Takeda, *Angew. Chem. Int. Ed.* **2011**, 50, 10157.

[71] H. Yoshida, Y. Kuwauchi, J. R. Jinschek, K. Sun, S. Tanaka, M. Kohyama, S. Shimada, M. Haruta, S. Takeda, *Science* **2012**, 335, 317.

[72] N. Ta, J. Liu, S. Chenna, P. A. Crozier, Y. Li, A. Chen, W. Shen, *J. Am. Chem. Soc.* **2012**, 134, 20585.

[73] Y. Kuwauchi, S. Takeda, H. Yoshida, K. Sun, M. Haruta, H. Kohno, *Nano Lett.* **2013**, 13, 3073.

[74] S. Zhang, C. Chen, M. Cargnello, P. Fornasiero, R. J. Gorte, G. W. Graham, X. Pan, *Nat. Commun.* **2015**, 6, 7778.

[75] a) W. van Aarle, W. J. Palenstijn, J. De Beenhouwer, T. Altantzis, S. Bals, K. J. Batenburg, J. Sijbers, *Ultramicroscopy* **2015**, 157, 35; b) J. C. Yang, M. W. Small, R. V. Grieshaber, R. G. Nuzzo, *Chem. Soc. Rev.* **2012**, 41, 8179.

[76] H. Friedrich, P. E. de Jongh, A. J. Verkleij, K. P. de Jong, *Chem. Rev.* **2009**, 109, 1613.

[77] X. Xu, Z. Saghi, G. Yang, R. J. Hand, G. Möbus, *Cryst. Growth Des.* **2008**, 8, 1102.

[78] a) C.-C. Chen, C. Zhu, E. R. White, C.-Y. Chiu, M. Scott, B. Regan, L. D. Marks, Y. Huang, J. Miao, *Nature* **2013**, 496, 74; b) Y. Yang, C.-C. Chen, M. Scott, C. Ophus, R. Xu, A. Pryor, L. Wu, F. Sun, W. Theis, J. Zhou, *Nature* **2017**, 542, 75; c) B. Goris, S. Bals, W. Van den Broek, E. Carbó-Argibay, S. Gómez-Graña, L. M. Liz-Marzán, G. Van Tendeloo, *Nat Mater* **2012**, 11, 930; d) S. Van Aert, K. J. Batenburg, M. D. Rossell, R. Erni, G. Van Tendeloo, *Nature* **2011**, 470, 374; e) K. H. W. van den Bos, A. De Backer, G. T. Martinez, N. Winckelmans, S. Bals, P. D. Nellist, S. Van Aert, *Phys. Rev. Lett.* **2016**, 116, 246101; f) S. Bals, M. Casavola, M. A. van Huis, S. Van Aert, K. J. Batenburg, G. Van Tendeloo, D. Vanmaekelbergh, *Nano Lett.* **2011**, 11, 3420.

[79] J. P. Y. Tan, H. R. Tan, C. Boothroyd, Y. L. Foo, C. B. He, M. Lin, *J. Phys. Chem. C* **2011**, 115, 3544.

[80] I. Florea, C. d. Feral-Martin, J. r. Majimel, D. Ihiawakrim, C. Hirlimann, O. Ersen, *Cryst. Growth Des.* **2013**, 13, 1110.

[81] C. Yang, F. Bebensee, J. Chen, X. Yu, A. Nefedov, C. Wöll, *ChemPhysChem* **2017**, 18, 1874.

[82] B. Goris, M. Meledina, S. Turner, Z. Zhong, K. J. Batenburg, S. Bals, *Ultramicroscopy* **2016**, 171, 55.

[83] S. M. Collins, S. Fernandez-Garcia, J. J. Calvino, P. A. Midgley, *Sci. Rep.* **2017**, 7, 5406.

[84] a) J. J. De Yoreo, N. Sommerdijk, *Nat. Rev. Mater.* **2016**, 1, 16035; b) H.-G. Liao, L. Cui, S. Whitelam, H. Zheng, *Science* **2012**, 336, 1011; c) M. H. Nielsen, S. Aloni, J. J. De Yoreo, *Science* **2014**, 345, 1158.

[85] a) J. M. Yuk, J. Park, P. Ercius, K. Kim, D. J. Hellebusch, M. F. Crommie, J. Y. Lee, A. Zettl, A. P. Alivisatos, *Science* **2012**, 336, 61; b) W.-I. Liang, X. Zhang, K. Bustillo, C.-H. Chiu, W.-W. Wu, J. Xu, Y.-H. Chu, H. Zheng, *Chem. Mater.* **2015**, 27, 8146.

[86] Q. Zhang, H. Li, L. Gan, Y. Ma, D. Golberg, T. Zhai, *Chem. Soc. Rev.* **2016**, 45, 2694.

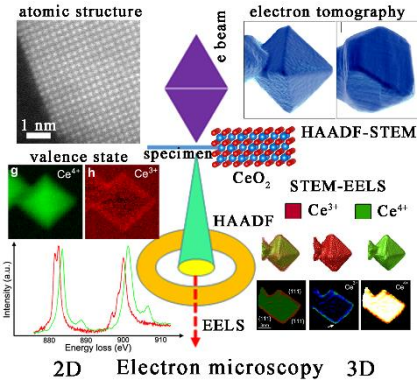

Apart from summarizing the basic physical and chemical properties of CeO_2-based nanostructures, emphasis is given to the contribution of TEM/STEM to study the relationship between composition, structure and property of these nanostructures. We conclude this review with critical comments, as well as some perspectives on future developments for a full characterization of CeO_2-based nanostructures is provided.

Sara Bals received her Ph.D. from the University of Antwerp in 2003 in the group of Prof. G. Van Tendeloo. From 2003–2004, she joined NCEM at the Lawrence Berkeley National Laboratory. Currently she is a Professor at EMAT, the electron microscopy group at the University of Antwerp. Her main research interest consists of the application and further development of electron tomography for advanced nanostructured materials. In 2013 she received an ERC Starting Grant.